

# Contributions to Mineralogy and Petrology

## Origin of pyroxenites in the oceanic mantle and their implications on the reactive percolation of depleted melts

--Manuscript Draft--

<b>Manuscript Number:</b>	
<b>Full Title:</b>	Origin of pyroxenites in the oceanic mantle and their implications on the reactive percolation of depleted melts
<b>Article Type:</b>	Original Paper
<b>Keywords:</b>	Pyroxenite; Melt-rock interaction; Mantle melting; pMELTS; Oceanic lithosphere; Alpine ophiolite
<b>Corresponding Author:</b>	Elisabetta Rampone, Ph.D. Universita' di Genova Genova, Italy ITALY
<b>Corresponding Author Secondary Information:</b>	
<b>Corresponding Author's Institution:</b>	Universita' di Genova
<b>Corresponding Author's Secondary Institution:</b>	
<b>First Author:</b>	V. Basch, Ph.D.
<b>First Author Secondary Information:</b>	
<b>Order of Authors:</b>	V. Basch, Ph.D. Elisabetta Rampone, Ph.D. G. Borghini, Ph.D. C. Ferrando, Ph.D. A Zanetti, Ph.D.
<b>Order of Authors Secondary Information:</b>	
<b>Funding Information:</b>	Ministero dell'Istruzione, dell'Università e della Ricerca (PRIN-2015C5LN35) Prof. Elisabetta Rampone
<b>Abstract:</b>	<p>Pyroxenites are diffuse in fertile mantle peridotites and considered an important component in the mantle source of oceanic basalts. They are rarely documented in abyssal and ophiolitic peridotites representing residual mantle after melt generation, and few studies defining their origin are to date available. We present a field-based microstructural and geochemical investigation of the pyroxenite layers associated to depleted peridotites from the Mt. Maggiore ophiolitic body (Corsica, France). Field and petrographic evidence indicate that pyroxenite formation preceded the melt-rock interaction history that affected this mantle sector during Jurassic exhumation, namely i) spinel-facies reactive porous flow leading to partial dissolution of the pyroxenites, and ii) plagioclase-facies melt impregnation leading to [plagioclase + orthopyroxene] interstitial crystallization. Pyroxenes show major element compositions similar to abyssal pyroxenites from slow-spreading ridges, indicative of magmatic segregation at pressures higher than 7 kbar. Both the parental melts of pyroxenites and the melts involved in the subsequent percolation were characterized by Na<sub>2</sub>O-poor, LREE-depleted compositions, consistent with unaggregated melt increments. This implies that they represent the continuous evolution of similarly depleted melts leading to different processes (pyroxenite segregation and later melt-rock interaction) during their upward migration. To support the genetic relation and the continuity between the formation of pyroxenites and the subsequent melt-rock interaction history, we modeled all the documented processes in sequence, i.e.: i) formation of single melt increments after 6% mantle decompressional fractional melting; ii) high-pressure segregation of pyroxenites; iii) spinel-facies reactive porous flow, iv) plagioclase-facies melt</p>

impregnation. The early fractionation of pyroxenites leads to a decrease in pyroxene saturation that is necessary for the subsequent reactive porous flow process, and accounts for the “pyroxene paradox”.

[Click here to view linked References](#)

1

1

2 2

3

4 3

5

6 4

7

8 5

9

10 6

11

12 7

13

14 8

15

16 9

17

18 10

19

20 11

21

22 12

23

24 13

25

26 14

27

28 15

29

30 16

31

32 17

33

34 18

35

36 19

37

38 20

39

40 21

41

42 22

43

44 23

45

46 24

47

48 25

49

50

51

52

53

54

55

56

57

58

59

60

61

62

63

64

65

**Origin of pyroxenites in the oceanic mantle and their implications on the  
reactive percolation of depleted melts**

**Basch, V.<sup>1</sup>; \*Rampone, E.<sup>1</sup>;**

<sup>1</sup>DISTAV, University of Genova, Italy

**Borghini, G.<sup>2</sup>;**

<sup>2</sup>Dipartimento di Scienze della Terra “Ardito Desio”, University of Milano, Italy

**Ferrando, C.<sup>3</sup>;**

<sup>3</sup>CRPG, University of Lorraine, Nancy, France

**Zanetti, A.<sup>4</sup>.**

<sup>4</sup>CNR-IGG, Sezione di Pavia, Italy

**Corresponding Author:**

**Elisabetta Rampone**

Dipartimento di Scienze della Terra, dell’Ambiente e della Vita (DISTAV)

Università degli Studi di Genova

Corso Europa 26

I-16132 Genova (Italy)

**Email:** [betta@dipteris.unige.it](mailto:betta@dipteris.unige.it)

27 **Abstract**

1  
28  
3  
49 Pyroxenites are diffuse in fertile mantle peridotites and considered an important component  
5  
30 in the mantle source of oceanic basalts. They are rarely documented in abyssal and ophiolitic  
7  
31 peridotites representing residual mantle after melt generation, and few studies defining their origin  
9  
32 are to date available. We present a field-based microstructural and geochemical investigation of the  
10  
133 pyroxenite layers associated to depleted peridotites from the Mt. Maggiore ophiolitic body (Corsica,  
12  
134 France). Field and petrographic evidence indicate that pyroxenite formation preceded the melt-rock  
14  
135 interaction history that affected this mantle sector during Jurassic exhumation, namely *i*) spinel-  
16  
36 facies reactive porous flow leading to partial dissolution of the pyroxenites, and *ii*) plagioclase-  
18  
37 facies melt impregnation leading to [plagioclase + orthopyroxene] interstitial crystallization.  
19  
2038 Pyroxenes show major element compositions similar to abyssal pyroxenites from slow-spreading  
21  
239 ridges, indicative of magmatic segregation at pressures higher than 7 kbar. Both the parental melts  
23  
240 of pyroxenites and the melts involved in the subsequent percolation were characterized by Na<sub>2</sub>O-  
25  
241 poor, LREE-depleted compositions, consistent with unaggregated melt increments. This implies  
27  
242 that they represent the continuous evolution of similarly depleted melts leading to different  
28  
2943 processes (pyroxenite segregation and later melt-rock interaction) during their upward migration.  
30  
3144 To support the genetic relation and the continuity between the formation of pyroxenites and the  
32  
345 subsequent melt-rock interaction history, we modeled all the documented processes in sequence,  
34  
346 i.e.: *i*) formation of single melt increments after 6% mantle decompressional fractional melting; *ii*)  
36  
347 high-pressure segregation of pyroxenites; *iii*) spinel-facies reactive porous flow, *iv*) plagioclase-  
38  
48 facies melt impregnation. The early fractionation of pyroxenites leads to a decrease in pyroxene  
39  
4049 saturation that is necessary for the subsequent reactive porous flow process, and accounts for the  
41  
4250 “pyroxene paradox”.

43  
4451  
45  
4652 **Keywords:** Pyroxenite; Melt-rock interaction; Mantle melting; pMELTS; Oceanic lithosphere;  
47  
4853 Alpine ophiolite.

## 54 Introduction

1  
2  
3  
4  
5  
6  
7  
8  
9  
10  
11  
12  
13  
14  
15  
16  
17  
18  
19  
20  
21  
22  
23  
24  
25  
26  
27  
28  
29  
30  
31  
32  
33  
34  
35  
36  
37  
38  
39  
40  
41  
42  
43  
44  
45  
46  
47  
48  
49  
50  
51  
52  
53  
54  
55  
56  
57  
58  
59  
60  
61  
62  
63  
64  
65

Pyroxenite bodies and/or layers are a minor but diffuse lithotype in fertile mantle peridotites and are considered an important component in the mantle source of oceanic basalts (e.g. [Hirschmann and Stolper 1996](#); [Stracke et al. 1999](#); [Salters and Dick 2002](#); [Kogiso et al. 2004a, 2004b](#); [Sobolev et al. 2005, 2007](#); [Lambart et al. 2013, 2016](#); [Borghini et al. 2017](#)). However, their origin remains a debated issue, since various magmatic and metamorphic processes can be invoked: *i*) metamorphic recycling of subducted oceanic crust incorporated into the lithosphere (e.g. [Allègre and Turcotte 1986](#); [Morishita and Arai 2001](#); [Morishita et al. 2003](#); [Yu et al. 2010](#)); *ii*) reactive melt percolation and “refertilization” of a depleted upper mantle during melt-peridotite interactions ([Garrido and Bodinier 1999](#); [Bodinier et al. 2008](#); [Dantas et al. 2009](#); [van Acken et al. 2010](#); [Laukert et al. 2014](#); [Borghini et al. 2013, 2016](#)); *iii*) moderate- to high-pressure melt segregation derived from asthenospheric melting ([Bodinier et al. 1987a, 1987b](#); [Vannucci et al. 1993](#); [Rivalenti et al. 1995](#); [Kempton and Stephens 1997](#); [Mukasa and Shervais 1999](#); [Takazawa et al. 1999](#); [Dantas et al. 2007](#); [Keshav et al. 2007](#); [Warren et al. 2009](#); [Gysi et al. 2011](#)).

Pyroxenites are commonly documented in association with fertile peridotites but only few studies have investigated pyroxenite layers and veins associated to depleted oceanic and ophiolitic peridotites representing residual mantle after partial melting of asthenospheric sources (e.g., [Dantas et al. 2007](#); [Warren et al. 2009](#); [Laukert et al. 2014](#)). These studies in oceanic settings inferred an origin of the pyroxenite layers as deep-seated (spinel-facies) magmatic segregations of depleted unaggregated melts and/or as replacive lithotypes after melt-rock interactions. Melt-rock interactions are increasingly invoked in extensional settings as key processes in modifying the modal and chemical composition of the host rock (lithospheric mantle and/or lower oceanic crust) and percolating melt (e.g. [Collier and Kelemen 2010](#); [Paquet et al. 2016](#); [Rampone et al. 2016, 2019](#); [Sanfilippo et al. 2016](#); [Basch et al. 2018, 2019](#); [Borghini et al. 2018](#); [Ferrando et al. 2018](#)). Therefore, the understanding of the origin of pyroxenites associated to residual peridotites and deciphering the melt-rock interaction processes is of utmost importance to constrain processes of melt production in oceanic environments, as well as the chemical evolution of melts during percolation through the oceanic lithosphere.

In the Mt.Maggiore ultramafic massif (Alpine Corsica, France), partially dissolved pyroxenite layers are associated with residual mantle peridotites that record a complex melt-rock interaction history from spinel-facies to plagioclase-facies conditions ([Rampone et al. 1997, 2008](#); [Müntener and Piccardo 2003](#); [Piccardo and Guarnieri 2010](#); [Basch 2018](#); [Basch et al. 2018](#)). Field evidence clearly indicate that pyroxenites preceded the latter melt migration stages. Previous geochemical

88 studies (Rampone et al. 1997, 2008; Piccardo and Guarnieri 2010; Basch et al. 2018) documented  
1  
289 that melts involved in the reactive percolation process have depleted compositions and likely  
3  
490 represent last melt increments formed at the top of a mantle column after 5-8% fractional melting of  
5  
691 a Depleted MORB Mantle source (DMM). The percolation of depleted melts in the oceanic  
7  
892 lithosphere has been extensively reported in slow-spreading oceanic setting, both in ophiolites  
9  
1093 (Rampone et al. 1997, 2008, 2019; Dijkstra et al. 2003; Piccardo et al. 2007; Rampone and  
11  
1294 Borghini, 2008; Sanfilippo and Tribuzio, 2011; Basch et al. 2018) and in modern mid-ocean ridges  
13  
1495 (Dantas et al. 2007; Dick et al. 2010; Warren and Shimizu 2010; Laukert et al. 2014). These  
15  
1696 peculiar melt compositions have been invoked as parental melts to pyroxenite layers from South-  
17  
1897 West Indian Ridge and Lena Trough (Dantas et al. 2007; Laukert et al. 2014). Records of depleted  
19  
2098 melts are mostly found in such relatively cold oceanic environments, as a result of a thick Thermal  
21  
2299 Boundary Layer and low melt production (e.g. Langmuir and Forsyth, 2007; Rampone et al. 2019)  
23  
2400 that does not allow for melt aggregation before extraction. Their composition and origin as  
25  
2601 unaggregated increments of fractional mantle melting has been well defined and modeled in terms  
27  
2802 of trace elements (e.g. Rampone et al. 2008; Basch et al. 2018) but little is known about their major  
29  
3003 element composition.

31  
3204 In this paper, we investigate the formation process of the Mt.Maggiore pyroxenite layers and  
33  
3405 its impact on the compositional evolution of percolating melts and the melt-rock interaction history.  
35  
3606 We used a multi-disciplinary approach combining field observations, microstructural and mineral  
37  
3807 major and trace element analyses. Our results were integrated with the melt-rock interaction history  
39  
4008 previously described in the host peridotites. Major outcomes of this study are: 1) the formation of  
41  
4209 the pyroxenites as early segregates from unaggregated depleted melts; 2) the necessity of pyroxene  
43  
4410 fractionation prior to the documented melt-rock interaction history, thus accounting for the  
45  
4611 “pyroxene paradox” (Francis 1986); 3) the demonstration of the evolution of reactive processes and  
47  
4812 chemical composition of depleted melts during upward migration in a thick Thermal Boundary  
49  
5013 Layer.

## 5116 **Structural and petrologic background**

52  
5317  
54  
5518 The Corsican peridotitic bodies are part of the Alpine-Apennine ophiolites, interpreted as the  
56  
5719 oceanic lithosphere remnants of the narrow Jurassic Ligurian Tethys basin. It was opened by  
58  
5920 passive lithosphere extension and ultimately led to slow- to ultra-slow spreading oceanization  
60  
6121 (20mm/year; e.g. Rampone et al. 2014). The Mt.Maggiore peridotitic massif is thought to represent

122 the base of the reconstructed “Schistes Lustrés” ophiolitic sequence exposed in the eastern Alpine  
123 Corsica (Jackson and Ohnenstetter 1981). Although it lacks any crustal cover, it preserves clear  
124 field relationships between mantle peridotites and associated pyroxenite and gabbroic intrusions.  
125 Previous geochemical studies demonstrated that clinopyroxenes in clinopyroxene-poor spinel  
126 lherzolites have relatively homogeneous LREE-depleted trace element compositions, consistent  
127 with residual mantle after low degrees (5–8%) of fractional melting (Rampone et al. 1997, 2008).  
128 The peridotitic body also records a subsequent multi-stage lithospheric exhumation history, through  
129 various episodes of melt-rock interaction from deep (spinel-facies) to shallower mantle depths  
130 (plagioclase-facies) (Müntener and Piccardo 2003; Piccardo and Guarnieri 2010; Rampone et al.  
131 1997, 2008; Basch et al. 2018).

132 A first event of olivine-saturated reactive melt percolation led to the dissolution of  
133 clinopyroxene and orthopyroxene, and crystallization of olivine at spinel-facies conditions. This  
134 melt-rock interaction is mostly recorded in reactive clinopyroxene-poor lherzolites and harzburgites  
135 by the development of olivine embayments partly replacing mantle orthopyroxene and  
136 clinopyroxene. Extensive reactive melt percolation led to the replacive formation of spinel dunite  
137 pods (e.g. Basch et al. 2018) and partial to complete dissolution of associated pyroxenite layers  
138 (Piccardo and Guarnieri 2010).

139 Plagioclase-bearing peridotites and troctolites show microstructural characteristics indicative of  
140 a plagioclase- ( $\pm$ opx) crystallizing, olivine-dissolving melt impregnation (Rampone et al. 1997,  
141 2008; Müntener and Piccardo 2003; Piccardo and Guarnieri 2010; Basch et al. 2018). Highly  
142 impregnated plagioclase peridotites often display plagioclase-rich gabbro-noritic veinlets,  
143 crystallized after segregation of the percolating melts. Rock-forming minerals in the gabbro-noritic  
144 veinlets (plagioclase, orthopyroxene and clinopyroxene) show LREE-depleted patterns, indicating a  
145 depleted composition of the impregnating melts. This melt composition has been previously  
146 described as consistent with depleted single melt increments formed after 5-8% of mantle fractional  
147 melting (Rampone et al. 1997, 2008; Basch et al. 2018), not corresponding to classical aggregated  
148 MORBs.

149 Together, the reported melt-rock interaction processes suggest open-system reactive  
150 percolation of olivine-saturated depleted melts at spinel-facies levels, followed by impregnation of  
151 the peridotites by depleted melts at shallower, colder lithospheric depths. Rampone et al. (2008) and  
152 Basch et al. (2018) described the progressive modification of the composition of percolating melt  
153 during upward migration. They inferred that melt-rock interaction occurring at spinel facies led to a  
154 progressive decrease in the olivine saturation and increase in pyroxene and plagioclase saturation.  
155 Therefore, the reaction-driven variation of the melt composition, together with the changes in

156 Pressure-Temperature conditions, enabled an evolution in the type of melt-rock interaction from an  
157 olivine-crystallizing, pyroxene-dissolving reactive melt percolation at spinel-facies to a plagioclase  
158 + orthopyroxene ± clinopyroxene melt impregnation at plagioclase-facies. This implies a continuity  
159 in the documented multi-stage melt-rock interaction history, tracking progressive exhumation of  
160 this mantle sector (Basch et al. 2018). Both spinel and plagioclase peridotites were intruded by later  
161 gabbroic dykes, ranging from olivine gabbros to diorites, showing MORB-type affinity (Piccardo  
162 and Guarnieri 2010).

## 163 164 **Field relationships and sampling**

165  
166 The Mt.Maggiore peridotitic massif (Corsica, France) is mainly composed of granular spinel  
167 and plagioclase peridotites, showing in places a weak NW-SE foliation marked by a preferential  
168 elongation of mantle pyroxenes (see Fig. 1 in Basch et al. 2018). The spinel peridotites show  
169 variations in modal compositions, ranging from clinopyroxene-poor lherzolites to olivine-rich  
170 harzburgites (up to 85 vol% olivine). In places, the spinel peridotites show diffuse to sharp contacts  
171 with metre-size spinel dunitic bodies. Mantle peridotites are associated to decimetre-size spinel  
172 pyroxenite layers (Fig. 1a) showing a constant NW-SE orientation throughout the ultramafic body,  
173 similar to the peridotite foliation (see Fig. 1 in Basch et al. 2018). In places, spinel pyroxenite layers  
174 are partially dissolved (Fig. 1b) and replaced by interstitial olivine (Fig. 1b,c). Within the dunite, the  
175 occurrence of aligned spinel trails also suggests the former presence of a pyroxenite layer, in which  
176 pyroxenes were completely dissolved during the spinel-facies reactive porous flow (Piccardo and  
177 Guarnieri 2010; Basch et al. 2018).

178 A recent study of the Mt.Maggiore peridotitic massif documented the presence of an  
179 impregnation front (Basch et al. 2018) on the field. The latter marks the transition from spinel  
180 peridotites and associated spinel pyroxenite layers to plagioclase-bearing peridotites and  
181 pyroxenites, showing enrichments in interstitial plagioclase and orthopyroxene (Fig. 1d,e). The  
182 most impregnated peridotites (up to 30 vol% interstitial plagioclase + orthopyroxene) show a  
183 steeply dipping (50–70°S) ESE-WNW modal layering of plagioclase enrichment and associated  
184 gabbroitic veinlets crosscutting the peridotite foliation and pyroxenite layers (Rampone et al.  
185 2008, 2019; Piccardo and Guarnieri 2010; Basch et al. 2018). All spinel- and plagioclase-bearing  
186 lithotypes are crosscut by steeply dipping gabbroic dikes (60–80°S), trending E-W to ESE-WNW.

## 187 188 **Sampling and analytical methods**



190 We sampled 8 pyroxenite layers, associated with both spinel and plagioclase peridotites (Table  
191 1). These pyroxenites are characterized by variable extents of pyroxene dissolution (Fig. 1b,c; Table  
192 1) and plagioclase-bearing impregnation (Fig. 1d,e). Although spinel pyroxenites (M11-6, M11-7,  
193 M11-7B, M11-8; associated with spinel peridotites; Fig. 1a,b) showed no sign of impregnation on  
194 the field, they all bear microstructural evidence of minor interstitial plagioclase and orthopyroxene  
195 (Fig. 1d,e; Table 1). Plagioclase pyroxenites (M11-4C, M11-5B, M11-12A, M11-12C; associated to  
196 plagioclase peridotites; Fig 1d,e) show stronger enrichments in impregnation-related phases  
197 (plagioclase up to 15 vol%).

198 We performed structural Electron Backscatter Diffraction (EBSD) mapping of all pyroxenite  
199 samples at Géosciences Montpellier (University of Montpellier, France). Mineral major element  
200 analyses (EPMA) have been performed at the Dipartimento di Scienze della Terra, University of  
201 Milano (Italy) and mineral trace element analyses (LA-ICP-MS) have been performed at C.N.R.,  
202 Istituto di Geoscienze e Georisorse, Unità di Pavia (Italy). Detailed methodologies for EBSD, major  
203 and trace elements analyses can be found in [Supplementary Material](#).

204 In the pyroxenites, clinopyroxenes and orthopyroxenes often show exsolutions of the conjugate  
205 pyroxene (see *Petrography*). Major element in-situ EPMA analyses were performed on mineral  
206 cores, rims and pyroxene exsolutions and are further referred to as “punctual analyses”. In order to  
207 reconstruct the major element composition of primary pyroxene porphyroclasts, prior to the  
208 subsolidus exsolution stage, we performed areal quantitative analyses of exsolved clinopyroxene  
209 and orthopyroxene porphyroclastic cores, from 100x100  $\mu\text{m}$  to 300x300  $\mu\text{m}$  (Fig. S1). The areal  
210 analyses that respect the stoichiometry of the bulk mineral (clinopyroxene or orthopyroxene) are  
211 used as a reference for the primary composition of the pyroxene core. These analyses have been  
212 performed at the Dipartimento di Scienze della Terra, dell’Ambiente e della Vita (DISTAV),  
213 University of Genoa using a TESCAN VEGA3 Scanning Electron Microscope equipped with an  
214 Energy Dispersive X-ray analyser (accelerating power 20kV).

## 215 **Petrography of the pyroxenite layers**

216 The pyroxenite layers are mainly websterites (Table 1). The primary mineral assemblage  
217 consists of coarse-grained clinopyroxene, orthopyroxene and spinel (Figs. 1,2). Clinopyroxenes are  
218 coarse porphyroclasts, partially corroded by interstitial olivine (Fig. 2a). They are deformed, as  
219 evidenced by undulatory extinction, and display exsolutions of variable sizes, from thin lamellas of  
220 orthopyroxene (Figs. 2e, S1) to 100 $\mu\text{m}$ -size orthopyroxene + plagioclase aggregates (Fig. 2f).  
221 Orthopyroxenes are found in two different microstructural situations: *i*) coarse porphyroclasts

224 partially corroded by interstitial olivine (opx1, [Fig. 2b](#)), showing undulatory extinctions and thin  
225 lamellas of clinopyroxene exsolutions ([Fig. S1](#)), and *ii*) interstitial to poikilitic orthopyroxene,  
226 associated to interstitial plagioclase, often forming orthopyroxene + plagioclase intergrowths (opx2,  
227 [Fig. 2c,d](#)). Interstitial orthopyroxene is mainly observed in the plagioclase pyroxenite samples  
228 showing extensive impregnation features (M11-5B, M11-12A, M11-12C). These interstitial  
229 orthopyroxenes are mostly undeformed and show few to no exsolutions of clinopyroxene. Olivines  
230 are always interstitial, showing lobate contacts against clinopyroxene and orthopyroxene  
231 porphyroclasts ([Fig. 2a,b](#)). They are deformed and often display kink bands. Plagioclases are always  
232 undeformed and occur as interstitial to poikilitic crystals showing lobate contacts against both  
233 pyroxene porphyroclasts and interstitial olivine ([Fig. 2d](#)). In the pyroxenite layers, they are mostly  
234 replaced by low-grade alteration products ([Fig. 2c,d](#)). Spinel is mostly black to brownish granular  
235 millimetre-size crystals associated to porphyroclastic pyroxenes and partially dissolved by  
236 interstitial olivine and plagioclase.

237 The main petrological features characterizing the pyroxenite layers therefore indicate that: *i*)  
238 spinel-facies reactive porous flow led to the partial dissolution of the porphyroclastic pyroxenes and  
239 to the interstitial crystallization of olivine; *ii*) plagioclase-facies impregnation led to enrichments in  
240 interstitial plagioclase and orthopyroxene at the expense of the porphyroclastic pyroxenes and  
241 interstitial olivine; *iii*) the pyroxenites were partially reequilibrated to plagioclase-facies sub-solidus  
242 conditions.

## 243 244 **Crystallographic Preferred Orientation of olivine**

245  
246 Pyroxenite layers all show a clear olivine Crystallographic Preferred Orientation (CPO)  
247 pattern. Despite the large grain size, the well-defined patterns allow to investigate qualitatively the  
248 olivine CPO. [Figure 3](#) shows the modal composition, olivine CPO, and BA-index (representative of  
249 the qualitative CPO symmetry of the olivine [100] and [010] axes; [Mainprice et al. 2014](#)) of all the  
250 pyroxenite layer samples.

251 Olivines in the pyroxenite layers (plagioclase-bearing olivine websterites) are characterized by  
252 an axial-[010] CPO (BA-index < 0.45; [Mainprice et al. 2014](#); [Tommasi and Ishikawa 2014](#)), with  
253 [010] being the strongest axis orientation, normal to the pyroxenite layer plane ([Fig. 3](#)). Such axial-  
254 [010] olivine CPOs have been previously described in impregnated peridotites ([Ben Ismail et al.](#)  
255 [2001](#); [Le Roux et al. 2008](#); [Tommasi et al. 2008](#)), replacive olivine-rich gabbroic rocks ([Higgie and](#)  
256 [Tommasi 2012, 2014](#)) and experiments of melt segregation during deformation ([Holtzman et al.](#)  
257 [2003](#)). Recently, [Basch et al. \(2018\)](#) performed a microstructural study of the Mt. Maggiore

258 ultramafic body and interpreted the olivine axial-[010] CPO in reacted spinel peridotite (olivine-  
259 enriched harzburgite), spinel dunite, olivine-rich troctolite, and troctolite as an indicator of  
260 deformation in the presence of melt (Holtzman et al. 2003; Le Roux et al. 2008; Kaczmarek and  
261 Tommasi 2011).

262

263

264

265

266

267

268

269

270

271

272

273

274

275

276

277

278

279

280

281

282

283

284

285

286

287

288

289

290

291

292

293

294

295

296

297

298

299

300

301

302

303

304

305

306

307

308

309

310

311

312

313

314

315

## Major and trace element mineral compositions

Major and trace element compositions of clinopyroxene, orthopyroxene, spinel, olivine and plagioclase from the studied pyroxenite layers are reported in Table S1-5 of Supplementary Material.

**Clinopyroxene** porphyroclast punctual analyses (Table S1) are characterized by relatively high Al<sub>2</sub>O<sub>3</sub> concentrations, progressively decreasing at increasing Mg-value from cores (Mg# = 88.0-90.5 mol%; Al<sub>2</sub>O<sub>3</sub> = 4.57-7.24 wt%), to rims (Mg# = 89.3-91.4 mol%; Al<sub>2</sub>O<sub>3</sub> = 3.20-5.95 wt%), to clinopyroxene exsolutions within orthopyroxene (Fig. 4a; Mg# = 90.3-92.0 mol%; Al<sub>2</sub>O<sub>3</sub> = 2.24-4.88 wt%). All punctual analyses of clinopyroxene show low Na<sub>2</sub>O and TiO<sub>2</sub> (Fig. 4b; Na<sub>2</sub>O = 0.08-0.24 wt%; TiO<sub>2</sub> = 0.2-0.4 wt%), and high Cr<sub>2</sub>O<sub>3</sub> contents (Cr<sub>2</sub>O<sub>3</sub> = 0.7-1.3 wt%). Clinopyroxene areal analyses of exsolved cores show compositions similar to punctual core analyses in terms of Mg-value (Mg# = 89-89.6 mol%; Fig. 4a,b), Al<sub>2</sub>O<sub>3</sub> (5.96-7.07 wt%; Fig. 4a) and Na<sub>2</sub>O concentrations (0.08-0.16 wt%; Fig. 4b), but they show higher MgO (19.53-19.81 wt%) and FeO (4.26-4.36 wt%), and lower CaO (18.10-18.44 wt%) concentrations, consistent with the bulk clinopyroxene composition prior to orthopyroxene exsolution. Porphyroclastic cores (both areal and punctual analyses; Fig. 4a,b) show similar Mg-values, Al<sub>2</sub>O<sub>3</sub> compositions and lower Na<sub>2</sub>O contents relative to clinopyroxenes analysed in spinel peridotites from Mt.Maggiore (Basch et al. 2018) and in spinel websterites from the South-West Indian Ridge (Dantas et al. 2007). Clinopyroxenes analysed in variably reequilibrated plagioclase websterites from the Lena Trough (Fig. 4a,b) show a range of variation of Al<sub>2</sub>O<sub>3</sub> and Mg-value similar to the core-rim variation in the Mt.Maggiore pyroxenites but higher Na<sub>2</sub>O concentrations (Laukert et al. 2014). Trace element compositions of clinopyroxene porphyroclastic cores (Fig. 5a) show strong LREE depletion (Ce<sub>N</sub>/Sm<sub>N</sub> = 0.015-0.037) and flat MREE-HREE patterns (Yb<sub>N</sub> = 8.4-10.4 times C1), similar to clinopyroxenes analysed in plagioclase peridotites and gabbro-noritic veinlets from Mt.Maggiore (Rampone et al. 2008; Basch et al. 2018), plagioclase websterites from the Lena Trough (Laukert et al. 2014), and spinel websterites from the South-West Indian Ridge (Dantas et al. 2007). These LREE-depleted compositions do not correspond to a MORB-type composition (Fig. 5a), unlike clinopyroxenes

291 reported in websterites from the Internal Ligurian ophiolites (Sanfilippo and Tribuzio 2011) and in  
292 part of the websterites from the South-West Indian Ridge (Warren et al. 2009).

293 **Orthopyroxene** porphyroclast punctual analyses (Table S2) show high Mg-value, Al<sub>2</sub>O<sub>3</sub>, and  
294 Cr<sub>2</sub>O<sub>3</sub> contents in orthopyroxene cores (Fig. 4c,d; Mg# = 88.8-90.1 mol%; Al<sub>2</sub>O<sub>3</sub> = 2.22-4.90 wt%;  
295 Cr<sub>2</sub>O<sub>3</sub> = 0.47-0.95 wt%) and rims (Mg# = 88.7-90.1 mol%; Al<sub>2</sub>O<sub>3</sub> = 1.79-4.85 wt%; Cr<sub>2</sub>O<sub>3</sub> = 0.43-  
296 0.93 wt%). Orthopyroxene exsolutions in clinopyroxene show similar Mg-values, Cr<sub>2</sub>O<sub>3</sub>  
297 compositions (Mg# = 88.4-89.9 mol%; Cr<sub>2</sub>O<sub>3</sub> = 0.55-0.87 wt%; Fig. 4c,d), and lower Al<sub>2</sub>O<sub>3</sub>  
298 contents (Al<sub>2</sub>O<sub>3</sub> = 1.71-3.76 wt%; Fig. 4c,d) with respect to the orthopyroxene porphyroclastic  
299 cores and rims. Orthopyroxene porphyroclastic cores and rims show variable CaO concentrations  
300 (CaO = 0.6-1.4 wt%), as a function of the extent of clinopyroxene exsolution. Orthopyroxene areal  
301 analyses of exsolved porphyroclastic cores show higher CaO (CaO = 2.1-2.5 wt%) and lower SiO<sub>2</sub>  
302 contents (SiO<sub>2</sub> = 53.9-54.3 wt%) than the punctual porphyroclastic core analyses. Interstitial and  
303 poikilitic orthopyroxenes also show higher CaO contents in crystal cores (CaO = 1.0-2.5 wt%) and  
304 rims (CaO = 0.9-1.5 wt%) than the orthopyroxene porphyroclasts. The analysed orthopyroxene  
305 porphyroclastic core compositions are similar to the ones reported in plagioclase websterites from  
306 the Lena Trough (Fig. 4c,d; Laukert et al. 2014) and to orthopyroxenes analysed in the associated  
307 plagioclase peridotites from Mt.Maggiore (Fig. 4c,d; Basch et al. 2018). Porphyroclastic and  
308 interstitial orthopyroxene cores (Fig. 5b) all show rather strong LREE depletion (Ce<sub>N</sub>/Yb<sub>N</sub> = 0.001-  
309 0.003), and MREE-HREE concentrations (Yb<sub>N</sub> = 2.3-3.1 times C1) similar to orthopyroxenes  
310 analysed in spinel websterites from South-West Indian Ridge (Dantas et al. 2007), in plagioclase  
311 websterites from Lena Trough (Laukert et al. 2014) and in plagioclase peridotites from  
312 Mt.Maggiore (Basch et al. 2018).

313 **Plagioclase** cores (Table S3) are characterized by anorthite-rich compositions (An = 93.1-95.4  
314 mol%), consistent with their low Na<sub>2</sub>O concentrations (Na<sub>2</sub>O = 0.52-0.78 wt%). The Na<sub>2</sub>O contents  
315 decrease towards the rims of the crystals, leading to more anorthitic rim compositions (Na<sub>2</sub>O =  
316 0.32-0.52 wt%; An = 95.4 -97.1 mol%). Plagioclase cores all show strong LREE depletion  
317 (Ce<sub>N</sub>/Sm<sub>N</sub> = 0.08-0.15; Sm<sub>N</sub> = 0.45-0.55 times C1) similar to plagioclase compositions reported in  
318 plagioclase websterites from the Lena Trough (Laukert et al. 2014) and in the associated plagioclase  
319 peridotites from Mt.Maggiore (Basch et al. 2018).

320 **Olivine** (Table S4) shows a narrow compositional range in all pyroxenite layers, at high  
321 Forsterite contents (Fo = 88.9-90.2 mol%), similar to the olivine compositions reported in the  
322 associated spinel peridotites, plagioclase peridotites, spinel dunites and troctolites from  
323 Mt.Maggiore (Fo = 89.5-90.2 mol%; Basch et al. 2018).

324 **Spinel** (Table S5) shows variable compositions between spinel pyroxenite and plagioclase  
325 pyroxenite. In the spinel pyroxenites, spinels show Cr-values, Mg-values and TiO<sub>2</sub> contents (Cr# =  
326 15 mol%; Mg# = 72 mol%; TiO<sub>2</sub> = 0.12 wt%) similar to what was documented in spinel websterites  
327 from the South-West Indian Ridge (Dantas et al. 2007). In the plagioclase pyroxenites, spinels show  
328 higher Cr-values and TiO<sub>2</sub> contents (Cr# = 32-42 mol%; TiO<sub>2</sub> = 0.32-0.40 wt%) and lower Mg-  
329 values (Mg# = 62-67 mol%).

## 331 Geothermobarometric estimates

332  
333 Equilibration temperatures of the different stages recorded in the pyroxenite layers were  
334 obtained using two-pyroxene Fe-Mg geothermometers (Brey and Kohler 1990; Taylor 1998) and  
335 Ca-in-orthopyroxene geothermometer (Brey and Kohler 1990). The calculated equilibrium  
336 temperature estimates are representative of: *i*) the formation of the pyroxenite layers, using areal  
337 analyses of orthopyroxene and clinopyroxene as representative of their primary composition (Fig.  
338 S1); *ii*) the plagioclase-facies impregnation stage of the pyroxenite, using punctual analyses of  
339 interstitial orthopyroxenes cores (using Ca-in-opx geothermometer). These estimates are completed  
340 with coupled orthopyroxene-clinopyroxene cores from the gabbro-norite segregations found within  
341 the plagioclase peridotites (data after Rampone et al. 2008 and Basch et al. 2018); *iii*) the  
342 plagioclase-facies sub-solidus reequilibration, using variably exsolved punctual cores and rims of  
343 porphyroclastic clinopyroxene and orthopyroxene, and coupling clinopyroxene and orthopyroxene  
344 exsolutions (Fig. 2e,f).

345 Additionally, we obtained geobarometric estimates of the plagioclase-bearing equilibrium  
346 applying the FACE geobarometer to clinopyroxene-orthopyroxene-plagioclase-olivine association  
347 (Fumagalli et al. 2017). We emphasize, however, that the FACE geobarometer was calibrated using  
348 experimental data on plagioclase peridotite compositions (Borghini et al. 2010, 2011; Fumagalli et  
349 al. 2017), meaning that our equilibration pressure calculations for olivine-bearing gabbro-noritic  
350 compositions represent indicative pressure estimates. This mineralogical association is found in  
351 different microstructural occurrences giving pressure estimates of: *i*) plagioclase-facies  
352 impregnation stage of the pyroxenite represented by the gabbro-noritic segregation mineral cores  
353 (data after Rampone et al. 2008 and Basch et al. 2018); *ii*) plagioclase-facies sub-solidus  
354 reequilibration represented by the mineral reequilibrated rims in impregnated pyroxenites. We used  
355 porphyroclastic rims of clinopyroxene, rims of interstitial olivine, and rims of interstitial  
356 orthopyroxene and plagioclase; *iii*) advanced stages of sub-solidus reequilibration represented by  
357 large orthopyroxene + plagioclase exsolution aggregates (Fig. 2f). The clinopyroxene and olivine

358 considered in the calculation are the reequilibrated clinopyroxene at the contact with the exsolution  
359 and the rims of interstitial olivine.

360 The geothermobarometric estimates obtained are summarized in [Table 2](#). The areal analyses of  
361 porphyroclastic clinopyroxene and orthopyroxene, representative of the spinel-facies formation of  
362 the pyroxenites, yield the highest equilibrium temperatures of 1210-1300°C. The plagioclase-facies  
363 melt impregnation process is characterized by high equilibrium temperatures of 1080-1290°C, at  
364 pressures of 6.4-6.6 kbar. The high variability of the temperature estimates is the expression of  
365 different extents of exsolution of the interstitial orthopyroxene cores (lower temperatures represent  
366 higher extents of exsolution). The sub-solidus reequilibration calculated at the rims of the  
367 porphyroclastic and interstitial crystals yield lower equilibrium temperatures and pressures of 880-  
368 1080°C at 4.2-4.6 kbar. The more extensive sub-solidus reequilibration represented by the  
369 plagioclase + orthopyroxene exsolution is characterized by low equilibrium temperatures of 780-  
370 900°C at 2.9-3.1 kbar.

## 372 Discussion

### 374 What do the pyroxenite layers represent?

375  
376 Previous studies of the Mt.Maggiore peridotitic massif described a complex melt-rock  
377 interaction history recorded in the spinel and plagioclase peridotites, dunites and troctolites  
378 ([Rampone et al. 1997, 2008](#); [Müntener and Piccardo 2003](#); [Piccardo and Guarnieri 2010](#); [Basch et  
al. 2018](#)). The evidence that pyroxenite layers record the processes of melt-rock interaction  
379 documented in the associated peridotites (e.g., [Basch et al. 2018](#)), indicates that their formation  
380 predates the spinel- to plagioclase-facies melt-rock interaction history.

381  
382 In the studied pyroxenites, olivine is always interstitial and shows lobate contacts against  
383 clinopyroxene and orthopyroxene porphyroclasts ([Fig. 2a,b](#)). We thus infer that olivine is entirely  
384 the product of the spinel-facies reactive porous flow. The crystallization of olivine during the  
385 reactive porous flow process is also suggested by the axial-[010] olivine CPO measured in the  
386 pyroxenite layers ( $0.18 < \text{BA-index} < 0.43$ ; [Fig. 3](#)). Similar axial-[010] olivine CPO were reported  
387 in the most reacted spinel harzburgites and spinel dunites from Mt.Maggiore (BA-index < 0.5;  
388 [Basch et al. 2018](#)) and interpreted as a melt-assisted deformation feature associated to the spinel-  
389 facies reactive porous flow process.

390 Within the pyroxenite layers, melt impregnation led to the interstitial crystallization of  
391 plagioclase and orthopyroxene at the expense of olivine and clinopyroxene porphyroclasts ([Fig.](#)

392 2c,d). These microstructural observations imply that plagioclase (10-15 vol%; Table 1) and at least  
393 part of the orthopyroxene abundance measured in the pyroxenites (15-50 vol%; Table 1) are the  
394 products of melt impregnation at plagioclase-facies conditions. Based on microstructural and EBSD  
395 map observations, we thus infer that the pyroxenite layers were primarily formed by large  
396 porphyroclastic clinopyroxene (~ 60-90 vol%), porphyroclastic orthopyroxene (~ 10-30 vol%) and  
397 spinel (~ 0-10 vol%).

398 Pyroxene porphyroclast cores in the studied pyroxenites have Al<sub>2</sub>O<sub>3</sub> compositions (Fig. 4)  
399 similar to those of South-West Indian Ridge and Lena Trough websterites (Seyler et al. 2001;  
400 Dantas et al. 2007; Laukert et al. 2014). These oceanic pyroxenites associated to residual peridotites  
401 were interpreted as formed by relatively high-pressure melt segregations (>7 kbar; Dantas et al.  
402 2007; Laukert et al. 2014). Experimental studies of MORB crystallization evidenced the possible  
403 formation of websterites during fractional and equilibrium crystallization processes occurring at  
404 pressures of 7-10 kbar (e.g. Villiger et al. 2004, 2007; Husen et al. 2016). The crystallization of  
405 websterites (clinopyroxene-orthopyroxene-spinel) is related to early saturation of pyroxenes, as a  
406 result of the increasing stability of pyroxenes and decreasing stability of plagioclase at increasing  
407 pressure. Villiger et al. (2004) also documented an increase in Al<sub>2</sub>O<sub>3</sub> concentration in clinopyroxene  
408 and orthopyroxene with pressure (up to 7 wt% Al<sub>2</sub>O<sub>3</sub> in clinopyroxene at 10 kbar. We infer that the  
409 primary modal composition, and the high Al<sub>2</sub>O<sub>3</sub> contents and Mg-values in porphyroclastic  
410 pyroxenes forming the Mt.Maggiore pyroxenites resulted from high-pressure fractionation (8-10  
411 kbar) of a migrating melt.

412 The pyroxene porphyroclasts show Na<sub>2</sub>O-poor (Fig. 4b) and LREE-depleted compositions  
413 (Fig. 5a,b), indicative of depleted parental melts (Fig. S2). In terms of REE concentrations,  
414 computed melts in equilibrium with clinopyroxenes are consistent with single melt increments  
415 formed after 5-8% fractional melting of a Depleted Mantle source (Fig. S2; Jackson et al. 1990;  
416 Warren 2016), as proposed for the melts percolating in the host peridotites (Rampone et al. 2008;  
417 Basch et al. 2018). Similar origin was inferred for spinel websterites from the Southwest Indian  
418 Ridge (Dantas et al. 2007).

419 Interstitial plagioclase and orthopyroxene show Na<sub>2</sub>O-poor and LREE-depleted compositions  
420 (Fig. 5b,c), similar to the porphyroclastic pyroxenes forming the primary mineral assemblage. This  
421 suggests a depleted composition of the impregnating melt, as previously documented in the host  
422 impregnated plagioclase peridotites (Rampone et al. 1997, 2008, 2019; Basch et al. 2018).

423 In summary, both the parental melts of pyroxenites and the melts involved in the subsequent  
424 percolation were characterized by Na<sub>2</sub>O-poor, LREE-depleted compositions, consistent with  
425 unaggregated melt increments rather than aggregated MORBs (Figs. 4, 5). This implies that they

426 represent the continuous evolution of similar melts leading to different processes (pyroxenite  
427 segregation and later melt-rock interaction) during their upward migration at changing Pressure-  
428 Temperature conditions from spinel-facies to plagioclase-facies depths. Such a continuity of the  
429 processes implies not only a temporal but also a spatial evolution during percolation of the melts in  
430 a mantle column in exhumation. To support the genetic relation and the continuity between the  
431 formation of pyroxenites and the subsequent melt-rock interaction history, we modeled all the  
432 documented processes in sequence, i.e.: *i*) formation of single melt increments after 6% mantle  
433 decompressional fractional melting; *ii*) high-pressure segregation of pyroxenites; *iii*) spinel-facies  
434 reactive porous flow, *iv*) plagioclase-facies melt impregnation. We used the pMELTS  
435 thermodynamic program (Ghiorso et al. 2002) that allows to assess the evolution of the melt phase  
436 saturation and chemical composition, and the major element composition of the fractionated phases.

437 [Basch et al. \(2018\)](#) recently modeled the REE compositional evolution of depleted melts  
438 during the melt-rock interaction history documented at Mt.Maggiore. However, major element  
439 modeling of the formation of melt during decompressional melting and subsequent chemical  
440 evolution during percolation was never performed in oceanic environments. The Mt.Maggiore  
441 peridotitic massif provides a good field ([Fig. 1](#)) and microstructural control ([Fig. 2](#)) on the  
442 chronology of the different processes documented within the pyroxenites, thus allowing to test the  
443 described dynamic model.

444

### 445 **Formation of the depleted single melt increments**

446

447 In order to simulate decompressional mantle melting and major element composition of single  
448 melt increments during fractional melting, we performed a model of adiabatic decompression of a  
449 Depleted MORB Mantle (DMM; [Workman and Hart 2005](#)). An adiabatic temperature gradient (~  
450 0.8°C/km; e.g. [Hebert and Montési 2010](#)) is imposed to the DMM mantle, upwelling from 25 kbar,  
451 1400°C to 9 kbar, 1360°C. The adiabat crosses the DMM solidus at 13.6 kbar, 1372°C, therefore  
452 initiating the mantle melting process ([Fig. S3](#)). At 10 kbar, 1362°C, fractional melting reaches 6%  
453 ([Fig. S3](#)), which is consistent with the mineral compositions documented in the residual peridotites  
454 (e.g. [Rampone et al. 2008](#)) and to the parental melt involved in the formation of pyroxenites and  
455 melt-rock interaction history (e.g. [Basch et al. 2018](#)). At this depth (~ 30 km) we infer that the  
456 residual mantle was incorporated in the Thermal Boundary Layer (TBL) and started cooling  
457 conductively, which in turn led to the cessation of the melting process (e.g. [Langmuir et al. 1992](#);  
458 [Shen and Forsyth 1995](#); [Niu 1997](#); [Niu and Hékinian 1997](#); [Langmuir and Forsyth 2007](#); [Montési](#)  
459 [and Behn 2007](#); [D’Errico et. 2016](#)). The narrow range of pressure involving mantle melting (13.6 to

61  
62  
63  
64  
65



460 10 kbar) and the thick TBL inferred are consistent with the cold ultraslow-spreading environment  
461 described at Mt. Maggiore (e.g. [Rampone et al. 2014, 2019](#)).

462 In [Figure 6](#), we compare the chemical evolution of single melt increments and aggregated  
463 melts along progressive melting. At increasing degree of melting, the melt compositions show  
464 decreasing concentrations of  $\text{Al}_2\text{O}_3$ ,  $\text{Na}_2\text{O}$  and increasing  $\text{SiO}_2$ ,  $\text{CaO}$  and  $\text{Ca\#}$  ( $\text{Ca\#} = \text{Ca}/(\text{Ca}+\text{Na})$   
465 mol%). Single melt increments show larger compositional variations than the aggregated melts,  
466 which are calculated as weighted mass balance of the different single melt increments ([Figure 6](#);  
467 [Table S6](#)). Both single melt increments and aggregated melts show high  $\text{Mg\#}$  (~ 75-76 mol%),  
468 consistent with primitive MORB compositions and/or unaggregated melts formed by multi-stage  
469 melting processes, as previously reported in experimental mantle melting studies ([Duncan and](#)  
470 [Green 1987](#); [Falloon and Green 1988](#); [Kinzler and Grove 1992](#); [Hirose and Kushiro 1993](#)) and in  
471 natural samples and melt inclusions ([Duncan and Green 1980](#); [Sobolev and Shimizu 1993](#)). The  
472 strongest compositional differences are observed for  $\text{Na}_2\text{O}$ ,  $\text{CaO}$  and therefore  $\text{Ca\#}$ , that is much  
473 higher in the single melt increments, respect to the aggregated melts (+15 mol% after 6% total  
474 melting). The composition of the selected melt, i.e. single melt increment after 6% of DMM melting  
475 (light red stripe in [Fig. 6](#)) is given in [Table 3](#) and shows high  $\text{Mg}$ -value ( $\text{Mg\#} = 75$  mol%),  $\text{CaO}$ -rich  
476 ( $\text{CaO} = 13$  wt%),  $\text{Na}_2\text{O}$ -poor compositions ( $\text{Na}_2\text{O} = 0.7$  wt%), consistently with the melt  
477 compositions documented at Mt.Maggiore ([Basch et al. 2018](#)).

### 479 **High-pressure segregation of the pyroxenite layers**

481 In order to constrain the magmatic formation of the pyroxenite layers, we performed a model  
482 of high-pressure reactive fractional crystallization. We used as starting melt composition the single  
483 melt increment calculated in the previous modeling stage after 6% DMM melting ([Table 3](#)). This  
484 melt fraction forms at 1362°C, 10 kbar while the mantle enters the TBL. We model the reactive  
485 fractional crystallization of this melt during its percolation in the lithospheric mantle from 10 kbar  
486 to 9.5 kbar, at temperatures decreasing from 1360°C to 1310°C. The temperatures assumed for the  
487 model are slightly higher than the geothermometric estimates obtained for porphyroclastic pyroxene  
488 pairs (up to 1300°C; [Table 2](#)). We infer that the difference between the modeled and calculated  
489 temperatures is the result of analytical uncertainty in the measurement of areal analyses and in the  
490 geothermometric estimates. The selected melt is only saturated in clinopyroxene at the pressures  
491 considered in our model. This model assumes the assimilation of 0.2 g/°C of host lherzolite  
492 (ol:opx:cpx:spinel = 58:27:12:3; computed by pMELTS). Small amounts of mantle assimilation are  
493 necessary in our model to reach orthopyroxene saturation in the melt. We infer that the reactivity of

494 this melt towards the host lherzolite is the result of the decompression and cooling of these newly  
495 formed melts. Such a model of reactive melt percolation assuming the assimilation of a bulk  
496 peridotite have been previously proposed by [Dijkstra et al. \(2003\)](#), [Collier and Kelemen \(2010\)](#) and  
497 [Sanfilippo et al. \(2016\)](#) to simulate deep melt percolation within the mantle.

498 **Figure 7** shows the modal composition of the crystallized and assimilated mineral phases in the  
499 reactive fractional crystallization model. After 20% fractionation at 1335°C (**Fig. 7a**), the melt  
500 crystallizes a spinel websterite formed by clinopyroxene (~ 80 vol%), orthopyroxene (~ 15 vol%),  
501 spinel (~ 3 vol%), and minor olivine (~ 2 vol%) (**Fig. 7b**). The computed modal compositions  
502 reproduce well the inferred modal compositions of the primary pyroxenite layers at Mt.Maggiore.  
503 The ratio mass assimilated / mass crystallized remains low and rather constant during the whole  
504 process of reactive fractional crystallization ( $M_a/M_c \sim 0.2$ ; **Fig. 7b**), and thus indicates that the  
505 process is dominated by melt fractionation, at decreasing melt mass.

506 The clinopyroxene and orthopyroxene compositions (**Table S6**) computed after 20%  
507 fractionation of the melt at 1335°C (**Fig. 8**) fit the areal analyses of porphyroclastic clinopyroxene  
508 and orthopyroxene analyzed in the Mt.Maggiore pyroxenites (**Tables S1, S2**). Punctual analyses of  
509 clinopyroxene porphyroclastic cores (**Fig. 8c,d; Table S1**) show lower MgO and FeO concentrations  
510 and higher CaO contents as a result of extensive orthopyroxene exsolution, and therefore are not  
511 reproduced by the model. We emphasize the importance of the use of areal analyses of the  
512 porphyroclastic pyroxene cores to reconstruct their primary composition (**Fig. S1**). Yet,  
513 discrepancies are observed between the areal analyses and the computed  $Al_2O_3$  concentrations in  
514 orthopyroxene, which is overestimated by pMELTS modeling (**Fig. 8e**). It is worth noting that  
515 pMELTS thermodynamic models ([Ghiorso et al. 2002](#)) do not integrate  $Cr_2O_3$  in pyroxenes and  
516 given the high  $Cr_2O_3$  concentration in porphyroclastic orthopyroxenes (**Fig. 4d**), a substitution of  
517  $Cr_2O_3$  by  $Al_2O_3$  in the modeled orthopyroxene M1 site would lead to a large computational error.  
518 Our modeling thus shows that the Mt.Maggiore pyroxenites correspond in terms of modal and  
519 chemical compositions (**Figs. 7,8**) to spinel websterites formed by reactive fractional crystallization  
520 after 20% fractionation of depleted melts at 1335°C.

## 521 522 **Spinel-facies reactive porous flow**

523  
524 In order to simulate the reactive porous flow process occurring at spinel facies, leading to  
525 partial dissolution of pyroxene porphyroclasts and crystallization of interstitial olivine (**Fig. 2a,b**)  
526 we performed a model of reactive fractional crystallization from 8 kbar to 7 kbar, at temperatures  
527 decreasing from 1320°C to 1290°C. We used as initial melt composition the computed melt after

528 formation of the pyroxenite at 1335°C in the previous model (Table 3). Based on microstructural  
529 constraints (Fig. 2a,b), this model assumes the assimilation of 0.1 g/°C of porphyroclastic  
530 pyroxenes (75% orthopyroxene, 25% clinopyroxene). The melt reactivity is related to the expansion  
531 of the olivine stability field at decreasing pressure (Kelemen 1990).

532 Figure 9 shows the modal composition of the products and assimilated phases of the reactive  
533 porous flow process. While temperature decreases from 1320 to 1290°C, the percolating melt  
534 assimilates a total of 3g of pyroxenes (2.25g orthopyroxene, 0.75g clinopyroxene) and fractionates  
535 4.5g of olivine (Fig. 9a; Table S6). This implies a rather high Ma/Mc of ~ 0.6-0.7 (Fig. 9b) and an  
536 almost constant liquid mass during the reactive porous flow process (Table S6), consistently with  
537 what was described in previous studies (Rampone et al. 2008; Basch et al. 2018). The low amount  
538 of assimilation and fractionation of the melt along the process (Fig. 9a) is also consistent with the  
539 microstructural evidence of a reactive porous flow process integrated over time (Basch et al. 2018),  
540 i.e. each single portion of melt percolating through the matrix leads to only part of the dissolution-  
541 precipitation process observed in the pyroxenite and peridotite. The composition of the olivine  
542 fractionated from the melt is almost constant during the modeled process (Fo = 89.5-90.0 mol%;  
543 Table S6) and corresponds to the composition of olivines analyzed in the pyroxenites and  
544 peridotites at Mt. Maggiore (Table S4; Rampone et al. 1997, 2008; Müntener and Piccardo 2003;  
545 Piccardo and Guarnieri 2010; Basch et al. 2018).

546 We attempted to perform this pMELTS thermodynamic model using as initial melt  
547 composition the 6% depleted single melt increment (Table 3), without considering the previous  
548 stage of high-pressure segregation of the pyroxenite layers. The results of this model are shown in  
549 Figure S4 and indicate the saturation of clinopyroxene at 1305°C, and therefore the formation of a  
550 wehrlite at decreasing temperatures (70 vol% clinopyroxene, 30 vol% olivine at 1285°C; Fig. S5b).  
551 This does not correspond to the microstructural observations of partial dissolution of pyroxenes and  
552 crystallization of interstitial olivine related to reactive porous flow (Fig. 2a,b). This implies that the  
553 early stage of fractionation of the pyroxenite layers at high pressure is necessary to decrease the  
554 pyroxene saturation in the melt during its decompressional evolution.

555 Previous studies of the melt-rock interaction history at Mt. Maggiore investigated the REE  
556 evolution of depleted melts during the processes of spinel-facies reactive porous flow and melt  
557 impregnation (Rampone et al. 2008; Piccardo and Guarnieri 2010; Basch et al. 2018). However,  
558 these studies did not consider the early fractionation of pyroxenites in the melt REE evolution. We  
559 performed a simple Assimilation-Fractional Crystallization (AFC) REE model (DePaolo 1981) of  
560 the high-pressure formation of pyroxenite layers, in order to assess its impact on the initial depleted  
561 melt REE composition. We assume 20% fractionation of the depleted melt (melt REE composition

562 after [Basch et al. 2018](#)), during assimilation of the country lherzolite at  $Ma/Mc = 0.2$  (mineral  
563 compositions after [Basch et al. 2018](#)). [Figure S5](#) shows that pyroxenite segregation does not lead to  
564 significant modification in the REE composition of the percolating melt ( $Ce_N/Yb_N$  from 0.16 to  
565 0.17;  $Yb_N$  from 15.7 to 17.2 times  $C1$ ). Therefore, the early formation of pyroxenites does not affect  
566 the previously described REE trace element evolution during reactive porous flow and impregnation  
567 processes ([Basch et al. 2018](#)).

568

569

### Plagioclase-facies melt impregnation

570

571

572

573

574

575

576

577

578

579

580

581

582

583

584

585

586

587

588

589

590

591

592

593

594

59

60

61

62

63

64

65

We simulated the melt impregnation stage documented in the peridotites and pyroxenites assuming a stage of melt reactive fractional crystallization from 7 kbar, 1280°C to 6 kbar, 1200°C. These conditions are consistent with our geothermobarometric estimates of the impregnation process ([Table 2](#)), indicating temperatures up to 1290°C, at pressures of 6.4-6.6 kbar. We used as initial melt composition the computed melt after the previous model of reactive porous flow at 1290°C ([Table 3](#)). Based on microstructural constraints ([Fig. 2c,d](#)), this model assumes the assimilation of 0.2 g/°C of cooling of interstitial olivine  $Fo_{90}$ .

[Figure 10](#) represents the modal composition of the products and assimilated phases during the melt impregnation model. The latter leads to an extensive crystallization of a gabbronoritic assemblage at first (plagioclase, orthopyroxene, clinopyroxene,  $\sim 10g/5^\circ C$  until 1260°C; [Fig. 10a](#)) and is then dominated by the crystallization of plagioclase alone ( $<1260^\circ C$ ; [Fig. 10a](#)). The gabbronoritic modal composition of the high-temperature impregnation products ([Fig. 10b](#)) is consistent with the [plagioclase + orthopyroxene  $\pm$  clinopyroxene] character of the impregnation ([Fig. 2c,d](#)) and the occurrence of gabbronoritic veinlets within the most impregnated peridotites and pyroxenites ([Basch et al. 2018](#)).  $Ma/Mc$  is low ( $\sim 0.1-0.3$ ; [Fig. 10b](#)), implying that the melt mass and porosity decrease rapidly during the impregnation process, consistently with what was described in previous studies ([Rampone et al. 2008](#); [Basch et al. 2018](#)).

The major element compositions of interstitial plagioclase and orthopyroxene analyzed in the pyroxenites ([Tables S2,S3](#)) fit well to the compositions of plagioclase and orthopyroxene fractionated from the melt at 1270-1280°C in the pMELTS model ([Fig. 11](#)). Again, the largest discrepancy between the measured and computed mineral compositions is the  $Al_2O_3$  content in orthopyroxene ([Fig. 11a](#)). We infer that this mismatch is due to a pMELTS computational error as previously discussed (see *Discussion 9.3*). This model therefore reproduces the microstructural observations related to the stage of melt impregnation ([Fig. 10](#)) and the geochemical composition of

595 the mineral phases (plagioclase, orthopyroxene, clinopyroxene) as products of melt impregnation at  
596 1270-1280°C (Fig. 11).

597  
598

## 598 **Depleted melts in slow-spreading oceanic environments**

599  
600

### 600 *Melt migration in a thick Thermal Boundary Layer*

601  
602

601 The peridotites from Mt. Maggiore have been previously described as one of the few  
602 occurrences of oceanic mantle in the Alpine-Apennine ophiolites (e.g. Rampone et al. 2019). They  
603 record a multi-stage history of decompressional melting and subsequent melt-rock interactions,  
604 related to the opening of the ultraslow-spreading Ligurian Tethys basin (Fig. 12a). In this oceanic  
605 context, the pMELTS thermodynamic models developed in this study allowed to reconstruct the  
606 Pressure-Temperature evolution (Fig. S6), ranging from adiabatic decompression to conductive  
607 cooling in the oceanic lithosphere. The thermodynamic models define a cold thermal regime (Fig.  
608 S6), in which decompressional melting of the peridotite occurs over a restricted range of pressure  
609 (13.6-10 kbar), and stops at relatively high pressures (10 kbar ~ 30 km) while being incorporated  
610 into the TBL (Fig. S6; e.g. Langmuir and Forsyth 2007). In this thick TBL, high-temperature  
611 magmatic processes are followed by plagioclase-facies subsolidus reequilibration documented in  
612 the plagioclase-bearing assemblage within the peridotites and associated pyroxenites (780-1080°C,  
613 3-5 kbar; Table 2). Thick TBL have been described in slow-spreading ophiolitic (Müntener et al.  
614 2010; Sanfilippo et al. 2017; Rampone et al. 2018; Basch et al. 2019) and oceanic environments  
615 (Langmuir et al. 1992; Cannat 1996; Niu 1997; Kelemen et al. 2007; Langmuir and Forsyth 2007;  
616 Montési and Behn 2007; Dick et al. 2010; Hebert and Montési 2010; Warren and Shimizu 2010;  
617 Sleep and Warren 2014; D'Errico et al. 2016), consistent with the geodynamic context of the Mt.  
618 Maggiore peridotitic body and Ligurian Tethys basin (Fig. 12a). Deep conductive cooling in slow-  
619 spreading lithosphere favours the freezing of melts percolating in the shallow mantle.

620 Hebert and Montési (2010) modeled the depth of the crystallization front as a function of  
621 spreading rate at mid-ocean ridges. The crystallization front corresponds to the depth at which  
622 migrating melts experience extensive crystallization at the double saturation of plagioclase and  
623 clinopyroxene. At spreading rates comparable to those estimated for the Ligurian Tethys basin (20  
624 mm/yr full spreading rate; see Rampone et al. 2014 and cited references), their model predicts the  
625 depth of the crystallization front at 18 km (~ 6 kbar). This is consistent with our pMELTS models  
626 indicating double saturation of plagioclase and clinopyroxene and extensive crystallization rates at 7  
627 kbar (Fig. 10; see Discussion 9.5). Therefore, the pMELTS thermodynamic models developed in

60  
61  
62  
63  
64  
65

628 this study are in good agreement with the typical thermal architecture (Fig. S6) expected for a cold  
629 ultraslow-spreading environment (Fig. 12a).

630

### 631 *Continuous evolution of depleted melts in a mantle column*

632 The thermodynamic models evidence the continuity of the described processes and therefore a  
633 continuous evolution of the depleted initial melt composition, from the formation of the pyroxenite  
634 layers to the reactive porous flow and impregnation processes (Fig. S6). The major element  
635 pMELTS modeling demonstrated the necessity of including the early fractionation of pyroxenes in  
636 the melt evolution, leading to a decrease of pyroxene saturation in the melt (see Discussion 9.4; Fig.  
637 S5). This decreased saturation accounts for the pyroxene paradox and is crucial to model the  
638 following spinel-facies reactive porous flow process without reaching saturation of clinopyroxene  
639 (Fig. S5) and, therefore, to reproduce the microstructural observations of a pyroxene-dissolving,  
640 olivine-crystallizing reactive porous flow.

641 The continuity of these reactive processes occurring at different depths in the conductive  
642 lithosphere (Fig. S6) also implies a vertical evolution of the types of melt-rock interactions  
643 (Rampone et al. 2019). Therefore, all processes occur at the same time at different depths in a  
644 mantle column in exhumation (Fig. 12b). To form the microstructural assemblages observed in our  
645 samples (impregnated pyroxenite reequilibrated to sub-solidus plagioclase-facies conditions), a  
646 pyroxenite layer formed at 10 kbar needs to reach the Pressure-Temperature conditions that account  
647 for extensive sub-solidus reequilibration (800°C, 3 kbar; Table 3). The full spreading rate of the  
648 Ligurian Tethys has been estimated to be 20 mm/yr (Rampone et al. 2014), which, following the  
649 equations of McKenzie (1969) and Warren et al. (2009), corresponds to an exhumation rate of 12.7  
650 mm/yr. At this rate, a pyroxenite layer formed at relatively high pressure (10 kbar ~ 30km) would  
651 be exhumed to shallow depths (3 kbar ~ 9 km) in 1.6 Ma (Fig. 12b). Their formation and  
652 subsequent impregnation by depleted melts imply that generation of these melts is a continuous  
653 process characterized by steady-state isotherms over the estimated duration of mantle exhumation.  
654 Our models demonstrate that a single process of mantle adiabatic decompression governs the  
655 formation of depleted melts. Percolation of such depleted melts in turn drive all the documented  
656 reactive processes occurring in the thick oceanic lithosphere.

657

### 658 *Pyroxenites at ultraslow-spreading ridges and the pyroxene paradox*

659 The Mt. Maggiore pyroxenites, similar to what was documented for abyssal pyroxenites from  
660 the South-West Indian Ridge and Gakkel Ridge, originated as deep melt segregations from depleted  
661 melts (Dantas et al. 2007; Laukert et al. 2014). Our modelling shows that the same depleted melts

662  
663  
664  
665

662 subsequently percolated this mantle sector, originating reactive harzburgites and dunites (at spinel-  
663 facies depth) and impregnated peridotites (at plagioclase-facies depth) during progressive upward  
664 migration. As discussed by [Rampone et al. \(2019\)](#), we thus infer that the depleted signature of these  
665 melts is a primary feature, reflecting their origin as single depleted melt increments. Depleted melts  
666 are presently documented in oceanic and ophiolitic peridotites from ultraslow spreading  
667 environments only (e.g., [Dijkstra et al. 2003](#); [Dantas et al. 2007](#); [Piccardo et al. 2007](#); [Piccardo and](#)  
668 [Guarnieri 2010](#); [Basch et al. 2018](#)). At such settings, low melt production and thick TBL may  
669 favour the preservation of unaggregated last depleted melt increments formed at the top of an  
670 upwelling melting mantle column.

671 Our models demonstrate that the expansion of olivine stability field during upward migration  
672 of the depleted melts does not account alone for the spinel-facies reactive porous flow leading to  
673 dissolution of mantle pyroxenes (see *Discussion 9.4*). Thus, the early segregation of pyroxenitic  
674 components is a necessary process in lowering the pyroxene saturation in the migrating melt and  
675 could be fundamental in the formation of olivine-saturated pyroxene-undersaturated melts. The  
676 high-pressure fractionation of melts beneath mid-ocean ridges is also frequently invoked to account  
677 for the “pyroxene paradox” ([Francis 1986](#); [Grove et al. 1992](#); [Dantas et al. 2007](#)). Migration of  
678 unaggregated melts and high-pressure crystallization of pyroxenites are favoured in a thick TBL  
679 and are likely to be a common feature at ultra-slow spreading ridges, such as the South-West Indian  
680 Ridge and Lena Trough ([Dantas et al. 2007](#); [Laukert et al. 2014](#)).

## 681 682 **Summary and conclusions**

683  
684 This study investigates the formation of the pyroxenite layers associated to the residual  
685 peridotites of the Mt. Maggiore. Combined microstructural and geochemical analyses point to a  
686 magmatic formation of the pyroxenite, as part of the complex reactive percolation history of  
687 depleted single melt increments. We performed pMELTS models of this evolution as follows:

688 1) Formation of the depleted melts by fractional melting of a DMM in an ultraslow-spreading  
689 environment, in which the thick TBL terminates the melting process at rather high pressure  
690 (10kbar);

691 2) Reactive crystallization of the pyroxenite layers (75% clinopyroxene, 20% orthopyroxene,  
692 5% spinel) during fractionation of the depleted melt at depth ( $Mc = 20\%$ ), and assuming the  
693 assimilation of small quantities of host peridotite ( $Ma/Mc = 0.2$ ).

694 3) Spinel-facies reactive porous flow of the modified melt leads to the assimilation of  
695 pyroxenes and crystallization of interstitial olivine, without significant modification in the melt  
696 mass ( $Ma/Mc = 0.6-0.7$ ;  $Mc < 5\%$ ).

697 4) The percolation of the modified depleted melts at shallower levels leads to the crystallization  
698 of gabbro-noritic assemblages (plagioclase, orthopyroxene, clinopyroxene) at the expense of olivine  
699 ( $Ma/Mc = 0.1-0.2$ ) during impregnation of the peridotites and associated pyroxenites.

700 The formation of pyroxenite layers from unaggregated depleted melts in ultra-slow spreading  
701 environments testifies their importance in the geochemical evolution of the melt percolating in the  
702 oceanic lithosphere. The early fractionation of pyroxenites leads to a decrease in pyroxene  
703 saturation, thus accounting for the “pyroxene paradox” and in turn favouring the subsequent  
704 reactive porous flow process leading to the dissolution of mantle pyroxenes at spinel-facies.

705

## 706 **Acknowledgments**

707

708 We thank Paolo Campanella and Alessandra Gavoglio, Christophe Nevado and Doriane Delmas for  
709 realization of the thin section and high-quality polishing, as well as Fabrice Barou for assistance  
710 with the EBSD analyses, Andrea Risplendente for assistance with the EPMA. This research has  
711 been supported by the Italian Ministry of Education, University and Research (MIUR) through the  
712 grant [PRIN-2015C5LN35] “Melt–rock reaction and melt migration in the MORB mantle through  
713 combined natural and experimental studies”.

714

## 715 **References**

716

717 Allègre CJ, Turcotte DL (1986) Implications of a two-component marble-cake mantle. *Nature* 323:  
718 123–127.

719

720 Basch V (2018) Melt–rock interactions in the oceanic lithosphere: microstructural and petro-  
721 geochemical constraints from ophiolites. PhD thesis, Università degli Studi di Genova, doi:  
722 10.15167/basch-valentin\_phd2018-05-10.

723

724 Basch V, Rampone E, Crispini L, Ferrando C, Ildefonse B, Godard M (2018) From mantle  
725 peridotites to hybrid troctolites: textural and chemical evolution during melt–rock interaction  
726 history (Mt. Maggiore, Corsica, France). *Lithos* 323: 4–23, doi:10.1016/j.lithos.2018.02.025.

727

728  
729  
730  
731



- 728 Basch V, Rampone E, Crispini L, Ferrando C, Ildefonse B, Godard M (2019) Multi-stage reactive  
729 formation of troctolites in slow-spreading oceanic lithosphere (Erro-Tobbio, Italy): a combined field  
730 and petrochemical study. *Journal of Petrology*, doi: 10.1093/petrology/egz019.  
731  
732 Ben Ismail W, Barruol G, Mainprice D (2001) The Kaapvaal craton seismic anisotropy:  
733 petrophysical analyses of upper mantle kimberlite nodules. *Geophysical Research Letters* 28: 2497–  
734 2500, doi: 10.1029/2000GL012419.  
735  
736 Bodinier J-L, Fabries J, Lorand J-P, Dostal J, Dupuy C (1987a) Geochemistry of amphibole  
737 pyroxenite veins from the Lherz and Freychinede ultramafic bodies (Ariege, French Pyrenees).  
738 *Bulletin de Minéralogie* 110: 345–358.  
739  
740 Bodinier J-L, Guiraud M, Fabries J, Dostal J, Dupuy C (1987b) Petrogenesis of layered pyroxenites  
741 from the Lherz, Freychinede and Prades ultramafic bodies (Ariege, French Pyrenees). *Geochimica*  
742 *et Cosmochimica Acta* 51: 279–290.  
743  
744 Bodinier J-L, Garrido CJ, Chanefo I, Bruguier O, Gervilla F (2008) Origin of pyroxenite–peridotite  
745 veined mantle by refertilization reactions: Evidence from the Ronda peridotite (Southern Spain).  
746 *Journal of Petrology* 49: 999–1025.  
747  
748 Borghini G, Fumagalli P, Rampone E (2010) The stability of plagioclase in the upper mantle:  
749 subsolidus experiments on fertile and depleted lherzolite. *Journal of Petrology* 51: 229-254.  
750  
751 Borghini G, Fumagalli P, Rampone E (2011) The geobarometric significance of plagioclase in  
752 mantle peridotites: A link between nature and experiments. *Lithos* 126: 42-53.  
753  
754 Borghini G, Rampone E, Zanetti A, Class C, Cipriani A, Hofmann AW, Goldstein SL (2013)  
755 Meter-scale Nd isotopic heterogeneity in pyroxenite-bearing Ligurian peridotites encompasses  
756 global-scale upper mantle variability. *Geology* 41: 1055-1058.  
757  
758 Borghini G, Rampone E, Zanetti A, Class C, Cipriani A, Hofmann AW, Goldstein SL (2016)  
759 Pyroxenite Layers in the Northern Apennines’ Upper Mantle (Italy)—Generation by Pyroxenite  
760 Melting and Melt Infiltration. *Journal of Petrology* 57: 625-653.

61  
62  
63  
64  
65

- 762 Borghini G, Fumagalli P, Rampone E (2017) Partial melting of secondary pyroxenite at 1 and 1.5  
763 GPa, and its role in upwelling heterogeneous mantle. *Contributions to Mineralogy and Petrology*  
764 172: 70, doi: 10.1007/s00410-017-1387-4.  
765  
766 Borghini, G, Francomme JE, Fumagalli P (2018) Melt–dunite interactions at 0.5 and 0.7 GPa:  
767 experimental constraints on the origin of olivine-rich troctolites. *Lithos* 323: 44–57.  
768  
769 Brey GP, Köhler T (1990) Geothermobarometry in four phase lherzolites II. New  
770 thermobarometers, and practical assessment of existing thermobarometers. *Journal of Petrology* 31:  
771 1353–1378.  
772  
773 Cannat M (1996) How thick is the magmatic crust at slow spreading ridges? *Journal of Geophysical*  
774 *Research Solid Earth* 101: 2847-2857.  
775  
776 Collier ML, Kelemen PB (2010) The case for reactive crystallization at Mid-Ocean ridges. *Journal*  
777 *of Petrology* 51: 1913–1940, doi: 10.1093/petrology/egq043.  
778  
779 Dantas C, Ceuleneer G, Gregoire M, Python M, Freydier R, Warren J, Dick HJB (2007)  
780 Pyroxenites from the Southwest Indian Ridge, 9–16°E: cumulates from incremental melt fraction  
781 produced at the top of a cold melting regime. *Journal of Petrology* 48: 647–660.  
782  
783 Dantas C, Gregoire M, Koester E, Conceicao RD, Rieck N (2009) The lherzolite–websterite  
784 xenolith suite from Northern Patagonia (Argentina): evidence of mantle–melt reaction processes.  
785 *Lithos* 107: 107–120.  
786  
787 De Paolo DJ (1981) Trace elements and isotopic effects of combined wall rock assimilation and  
788 fractional crystallization. *Earth Planetary Science Letters* 53: 189–202.  
789  
790 D'Errico ME, Warren JM, Godard M (2016) Evidence for chemically heterogeneous Arctic mantle  
791 beneath the Gakkel ridge. *Geochimica et Cosmochimica Acta* 174: 291–312, doi:  
792 10.1016/j.gca.2015.11.017.  
793

- 794 Dick HJB, Lissenberg CJ, Warren JM (2010) Mantle melting melt transport, and delivery beneath a  
1  
795 slow-spreading ridge: the paleo-MAR from 23°15'N to 23°45'N. *Journal of Petrology* 51: 425-467,  
2  
796 doi: 10.1093/petrology/egp088.  
3  
4  
5  
6  
797  
798 Dijkstra AH, Barth MG, Drury MR, Mason PRD, Vissers RLM (2003) Diffuse porous melt flow  
8  
799 and melt-rock reaction in the mantle lithosphere at a slow-spreading ridge: a structural petrology  
10  
800 and LA-ICP-MS study of the Othris peridotite massif (Greece). *Geochemistry, Geophysics,*  
12  
801 *Geosystems* 4: 8613, doi: 10.1029/ 2001GC000278.  
14  
802  
15  
16  
803 Duncan RA, Green DH (1980) The role of multi-stage melting in the formation of the oceanic crust.  
17  
804 *Geology* 8: 22-26.  
19  
805  
21  
806 Duncan RA, Green DH (1987) The genesis of refractory melts in the formation of oceanic crust.  
23  
807 *Contributions to Mineralogy and Petrology* 96: 326-342.  
24  
25  
808  
26  
27  
809 Falloon TJ, Green DH (1988) Anhydrous partial melting of peridotite from 8 to 35 kbars and the  
28  
810 petrogenesis of MORB. *Journal of Petrology, Lithosphere Special Volume*: 379-414.  
30  
811  
32  
812 Ferrando C, Godard M, Ildefonse B, Rampone E (2018) Melt transport and mantle assimilation at  
34  
813 Atlantis Massif (IODP Site U1309): constraints from geochemical modelling. *Lithos* 323: 24–43.  
35  
36  
814  
37  
38  
815 Francis D (1986) The pyroxene paradox in MORB glasses - a signature of picritic parental  
39  
816 magmas? *Nature* 319: 586-588.  
41  
817  
43  
818 Fumagalli P, Borghini G, Rampone E, Poli S (2017) Experimental calibration of Forsterite–  
45  
819 Anorthite–Ca-Tschermak-Enstatite (FACE) geobarometer for mantle peridotites. *Contributions to*  
46  
820 *Mineralogy and Petrology* 172: 38.  
47  
48  
49  
821  
50  
51  
822 Garrido CJ, Bodinier JL (1999) Diversity of mafic rocks in the Ronda peridotite: evidence for  
52  
823 pervasive melt– rock reaction during heating of subcontinental lithosphere by upwelling  
54  
824 asthenosphere. *Journal of Petrology* 40: 729–754.  
55  
56  
825  
57  
58  
59  
60  
61  
62  
63  
64  
65

826 Ghiorso MS, Hirschmann M, Reiners PW, Kress VCI (2002) The pMELTS: a revision of MELTS  
1  
827 aimed at improving calculation of phase relations and major element partitioning involved in partial  
2  
828 melting of the mantle at pressures up to 3 GPa. *Geochemistry, Geophysics, Geosystems* 3: 36.  
3  
4  
5  
829  
6  
830 Grove TL, Kinzler RJ, Brian WB (1992) Fractionation of mid-ocean ridge basalt. In: Morgan JP,  
7  
831 Blackman DK, Sinton JM (eds) *Mantle flow and melt generation at mid-ocean ridges*, Geophysical  
8  
9  
10  
832 Monograph, American Geophysical Union 71: 281-311.  
11  
12  
13  
833  
14  
834 Gysi AP, Jagoutz O, Schmidt MW, Targuisti K (2011) Petrogenesis of pyroxenites and melt  
15  
16  
835 infiltrations in the ultramafic complex of Beni Bousera, Northern Morocco. *Journal of Petrology* 52:  
17  
18  
836 1676–1735.  
19  
20  
837  
21  
838 Hebert LB, Montési LGJ (2010) Generation of permeability barriers during melt extraction at mid-  
22  
23  
839 ocean ridges. *Geochemistry, Geophysics, Geosystems* 11: Q12008, doi: 10.1029/2010GC003270.  
24  
25  
840  
26  
841 Higgin K, Tommasi A (2012) Feedbacks between deformation and melt distribution in the crust-  
27  
28  
842 mantle transition zone of the Oman ophiolite. *Earth and Planetary Science Letters* 359–360: 61–72.  
29  
30  
843 doi: 10.1016/j.epsl.2012.10.003.  
31  
32  
844  
33  
845 Higgin K, Tommasi A (2014) Deformation in a partially molten mantle: constraints from  
34  
35  
846 plagioclase lherzolites from Lanzo, western Alps. *Tectonophysics* 615–616: 167–181. doi:  
36  
37  
847 10.1016/j.tecto.2014.01.007.  
38  
39  
848  
40  
849 Hirose K, Kushiro I (1993) Partial melting of dry peridotites at high pressures: Determination of  
41  
42  
850 compositions of melts segregated from peridotite using aggregates of diamond. *Earth and Planetary  
43  
44  
851 Science Letters* 114: 477-489.  
45  
46  
852  
47  
48  
853 Hirschmann MM, Stolper EM (1996) A possible role for garnet pyroxenite in the origin of the  
49  
50  
854 “garnet signature” in MORB. *Contributions to Mineralogy and Petrology* 124: 185-208.  
51  
52  
855  
53  
856 Holtzman BK, Kohlstedt DL, Zimmerman ME, Heidelbach F, Hiraga T, Hustoft J (2003) Melt  
54  
55  
857 segregation and strain partitioning: implications for seismic anisotropy and mantle flow. *Science*  
56  
57  
858 301: 1227–1230, doi: 10.1126/science.1087132.  
58  
59  
859  
60  
61  
62  
63  
64  
65

860 Husen A, Renat RA, Holtz F (2016) The effect of H<sub>2</sub>O and Pressure on Multiple Saturation and  
861 Liquid Lines of Descent in Basalt from the Shatsky Rise. *Journal of Petrology* 57: 309-344, doi:  
862 10.1093/petrology/egw008.  
863  
864 Jackson MD, Ohnenstetter M (1981) Peridotite and gabbroic structures in the Monte Maggiore  
865 massif, Alpine Corsica. *Journal of Geology* 89: 703–719.  
866  
867 Johnson KTM, Dick HJB, Shimizu N (1990) Melting in the oceanic upper mantle: an ion  
868 microprobe study of diopsides in abyssal peridotites. *Journal of Geophysical Research* 95: 2661–  
869 2678, doi: 10.1029/JB095iB03p02661.  
870  
871 Kaczmarek MA, Tommasi A (2011) Anatomy of an extensional shear zone in the mantle, Lanzo  
872 massif, Italy. *Geochemistry, Geophysics, Geosystems* 12: Q0AG06, doi: 10.1029/2011GC003627.  
873  
874 Kelemen PB, Kikawa E, Miller DJ and Shipboard Scientific Party (2007) Leg 209 summary:  
875 processes in a 20-km thick conductive boundary layer beneath the Mid-Atlantic Ridge, 14°–16°N.  
876 In Kelemen PB, Kikawa E, Miller DJ (Eds.), *Proceedings of the Ocean Drilling Project, Scientific*  
877 *Results* 209: 1–33, College Station, TX (Ocean Drilling Program), doi:  
878 10.2973/odp.proc.sr.209.001.2007.  
879  
880 Kempton PD, Stephens CJ (1997) Petrology and geochemistry of nodular websterites inclusions in  
881 harzburgite, Hole 920D. In: Karson JA et al (eds) *Proceedings of the Ocean Drilling Program,*  
882 *Scientific Results* 153: 321-331, College Station, TX (Ocean Drilling Program).  
883  
884 Keshav S, Sen G, Presnall DC (2007) Garnet-bearing xenoliths from Salt Lake Crater, Oahu,  
885 Hawaii: high-pressure fractional crystallization in the oceanic mantle. *Journal of Petrology* 48:  
886 1681–1724.  
887  
888 Kinzler RJ, Grove TL (1992) Primary magmas of mid-ocean ridge basalts 1. Experiments and  
889 methods. *Journal of Geophysical Research* 97: 6907-6926.  
890  
891 Kogiso T, Hirschmann MM, Pertermann M. (2004a) High pressure partial melting of mafic  
892 lithologies in the mantle. *Journal of Petrology* 45: 2407–2422.

- 894 Kogiso T, Hirschmann MM, Reiners W (2004b) Length scales of mantle heterogeneities and their  
895 relationship to ocean island basalt geochemistry. *Geochimica et Cosmochimica Acta* 68: 345–360.  
896
- 897 Lambart S, Laporte D, Schiano P (2013) Markers of the pyroxenite contribution in the major-  
898 element compositions of oceanic basalts: Review of the experimental constraints. *Lithos* 160–161:  
899 14–36.  
900
- 901 Lambart S, Baker MB, Stolper EM (2016) The role of pyroxenite in basalt genesis: Melt-PX, a  
902 melting parameterization for mantle pyroxenites between 0.9 and 5 GPa. *Journal of Geophysical  
903 Research: Solid Earth* 121: 5708-5735.  
904
- 905 Langmuir CH, Forsyth DW (2007) Mantle melting beneath mid-ocean ridges. *Oceanography* 20:  
906 78-89.  
907
- 908 Langmuir CH, Klein EM, Plank T (1992) Petrological systematics of mid-ocean ridge basalts:  
909 Constraints on melt generation beneath ocean ridges. In: *Mantle Flow and Melt Generation at Mid-  
910 Ocean Ridges*. Phipps Morgan J, Blackman DK, Sinton JM (eds) American Geophysical Union,  
911 Washington, DC, pp. 183–280.  
912
- 913 Laukert G, Von der Handt A, Hellebrand E, Snow J, Hoppe P, Klugel A (2014) High-pressure  
914 reactive melt stagnation recorded in abyssal pyroxenites from the ultraslow-spreading Lena Trough,  
915 Arctic Ocean. *Journal of Petrology* 55: 427-458.  
916
- 917 Le Roux V, Tommasi A, Vauchez A (2008) Feedback between melt percolation and deformation in  
918 an exhumed lithosphere-asthenosphere boundary. *Earth and Planetary Science Letters* 274: 401–  
919 413, doi: 10.1016/j.epsl.2008.07.053.  
920
- 921 Mainprice D, Bachmann F, Hielscher R, Schaeben H (2014) Descriptive tools for the analysis of  
922 texture projects with large datasets using MTEX: strength, symmetry and components. *Geological  
923 Society of London, Special Publication* 409.  
924
- 925 McKenzie DP (1969) Speculations on the consequences and causes of plate motions, *Geophysical  
926 Journal of the Royal Astronomical Society* 18: 1–32.  
927

- 928 Montési LGJ, Behn MD (2007) Mantle flow and melting underneath oblique and ultraslow MORs,  
929 Geophysical Research Letters 34: L24307.
- 930
- 931 Morishita T, Arai S (2001) Petrogenesis of corundum-bearing mafic rock in the Horoman Peridotite  
932 Complex, Japan. *Journal of Petrology* 42: 1279–1299.
- 933
- 934 Morishita T, Arai S, Gervilla F, Green DH (2003) Closed system geochemical recycling of crustal  
935 materials in the upper mantle. *Geochimica et Cosmochimica Acta* 67: 303–310.
- 936
- 937 Mukasa SB, Shervais JW (1999) Growth of sub-continental lithosphere: Evidence from repeated  
938 injections in the Balmuccia lherzolite massif, Italian Alps. *Lithos* 48: 287–316.
- 939
- 940 Müntener O, Piccardo GB (2003) Melt migration in ophiolitic peridotites: the message from  
941 Alpine–Apennine peridotites and implications for embryonic ocean basin. In: Dilek Y, Robinson  
942 PT (eds) *Ophiolites in Earth History: Geological Society of London Special Publication* 218: 69–  
943 89.
- 944
- 945 Müntener O, Manatschal G, Desmurs L, Pettke T (2010) Plagioclase peridotites in Ocean-continent  
946 transitions: refertilized mantle domains generated by melt stagnation in the shallow mantle  
947 lithosphere. *Journal of Petrology* 51: 255-294.
- 948
- 949 Niu Y (1997) Mantle melting and melt extraction processes beneath ocean ridges: evidence from  
950 abyssal peridotites. *Journal of Petrology* 38: 1047–1074.
- 951
- 952 Niu Y, Hékinian R (1997) Spreading-rate dependence of the extent of mantle melting beneath ocean  
953 ridges. *Nature* 385: 326-329.
- 954
- 955 Paquet M, Cannat M, Brunelli D, Hamelin C, Humler E (2016) Effect of melt/mantle interactions  
956 on MORB chemistry at the easternmost southwest Indian ridge (61 to 67°E). *Geochemistry,  
957 Geophysics, Geosystems* 17: 4605–4640, doi: 10.1002/2016GC006385.
- 958
- 959 Piccardo GB, Zanetti A, Müntener O (2007) Melt-peridotite interaction in the southern Lanzo  
960 peridotite: field, textural and geochemical evidence. *Lithos* 94: 181-209.

- 962 Piccardo GB, Guarnieri L (2010) The Monte Maggiore peridotite (Corsica, France): a case study of  
963 mantle evolution in the Ligurian Tethys. *Geological Society of London* 337: 7–45, doi:  
964 10.1144/SP337.20305-8719/10.  
965  
966 Rampone E, Borghini G (2008) Melt migration and intrusion in the Erro–Tobbio peridotites  
967 (Ligurian Alps, Italy): insights on magmatic processes in extending lithospheric mantle. *European*  
968 *Journal of Mineralogy* 20: 573–585.  
969  
970 Rampone E, Piccardo GB, Vannucci R, Bottazzi P (1997) Chemistry and origin of trapped melts in  
971 ophiolitic peridotites. *Geochimica et Cosmochimica Acta* 61: 4557–4569.  
972  
973 Rampone E, Piccardo GB, Hofmann AW (2008) Multistage melt–rock interaction in the Mt.  
974 Maggiore (Corsica, France) ophiolitic peridotites: microstructural and geochemical records.  
975 *Contributions to Mineralogy and Petrology* 156: 453–475.  
976  
977 Rampone E, Borghini G, Romairone A, Abouchami W, Class C, Goldstein SL (2014) Sm–Nd  
978 geochronology of the Erro-Tobbio gabbros (Ligurian Alps, Italy): Insights into the evolution of the  
979 Alpine Tethys. *Lithos* 205: 236-246.  
980  
981 Rampone E, Borghini G, Godard M, Ildefonse B, Crispini L, Fumagalli P (2016) Melt/rock reaction  
982 at oceanic peridotite/gabbro transition as revealed by trace element chemistry of olivine.  
983 *Geochimica et Cosmochimica Acta* 190: 308-331.  
984  
985 Rampone E, Borghini G, Basch V (2019) Melt migration and melt–rock reaction in the Alpine–  
986 Apennine peridotites: insights on mantle dynamics in extending lithosphere. *Geoscience Frontiers*,  
987 doi: 10.1016/j.gsf.2018.11.001.  
988  
989 Rivalenti G, Mazzucchelli M, Vannucci R, Hofmann AW, Ottolini L, Obermiller W (1995) The  
990 relationship between websterite and peridotite in the Balmuccia peridotite massif (NW Italy) as  
991 revealed by trace element variations in clinopyroxene. *Contributions to Mineralogy and Petrology*  
992 121: 275–288.  
993  
994 Salters VJM, Dick HJB (2002) Mineralogy of the mid ocean ridge basalt source from neodymium  
995 isotopic composition of abyssal peridotites. *Nature* 418: 68–72.



996  
1  
997  
2  
998  
3  
4  
999  
5  
6  
1000  
7  
8  
1001  
9  
10  
1002  
11  
12  
1003  
13  
14  
1004  
15  
16  
1005  
17  
18  
1006  
19  
20  
1007  
21  
22  
1008  
23  
24  
1009  
25  
26  
1010  
27  
28  
1011  
29  
30  
1012  
31  
32  
1013  
33  
34  
1014  
35  
36  
1015  
37  
38  
39  
1016  
40  
41  
1017  
42  
43  
1018  
44  
45  
1019  
46  
47  
1020  
48  
49  
1021  
50  
51  
1022  
52  
53  
1023  
54  
55  
1024  
56  
57  
1025  
58  
59  
60  
61  
62  
63  
64  
65

Sanfilippo A, Tribuzio R (2011) Melt transport and deformation history in a nonvolcanic ophiolitic section, northern Apennines, Italy: implications for crustal accretion at slow-spreading settings. *Geochemistry, Geophysics, Geosystems* 12: Q0AG04, doi: 10.1029/2010GC003429.

Sanfilippo A, Dick HJB, Ohara Y, Tiepolo M (2016) New insights on the origin of troctolites from the breakaway area of the Godzilla Megamullion (Parece Vela back-arc basin): the role of melt-mantle interaction on the composition of the lower crust. *Island Arc* 25: 220–234, doi.org/10.1111/iar.12137.

Sanfilippo A, Tribuzio R, Ottolini L, Hamada M (2017) Water, lithium and trace element compositions of olivine from Lanzo South replacive mantle dunites (Western Alps): new constraints into melt migration processes at cold thermal regimes. *Geochimica et Cosmochimica Acta* 214: 51-72, doi: 10.1016/j.gca.2017.07.034.

Seyler M, Toplis MJ, Lorand JP, Luguet A, Cannat M (2001) Clinopyroxene microtextures reveal incompletely extracted melts in abyssal peridotites. *Geology* 29: 155-158.

Shen Y, Forsyth DW (1995) Geochemical constraints on initial and final depths of melting beneath ocean ridges. *Journal of Geophysical Research* 100: 2211–2237.

Sleep NH, Warren JM (2014) Effect of latent heat of freezing on crustal generation at low spreading rates. *Geochemistry, Geophysics, Geosystems* 15: 3161-3174.

Sobolev AV, Shimizu N (1993) Ultra-depleted primary melt included in an olivine from the Mid-Atlantic Ridge. *Nature* 363: 151-154.

Sobolev AV, Hofmann AW, Sobolev SV, Nikogosian IK (2005) An olivine-free mantle source of Hawaiian shield basalts. *Nature* 434: 590-597.

Sobolev AV, Hofmann AW, Kuzmin DV et al. (2007) The amount of recycled crust in sources of mantle-derived melts. *Science* 316: 412-417.

- 1029 Stracke A, Salters VJM, Sims KWW (1999) Assessing the presence of garnet-pyroxenite in the  
1030 mantle sources of basalts through combined hafnium–neodymium–thorium isotope systematics.  
1031 *Geochemistry, Geophysics, Geosystems* 1: 15.
- 1032
- 1033 Sun S-S, McDonough WF (1989) Chemical and isotopic systematics of oceanic basalts:  
1034 implications for mantle composition and processes. In: Saunders AD, Norry MJ (eds) *Magmatism*  
1035 *in the Ocean Basins*. Geological Society, London, Special Publications 42: 313-345.
- 1036
- 1037 Takazawa E, Frey FA, Shimizu N, Saal N, Obata M (1999) Polybaric petrogenesis of mafic layers  
1038 in the Horoman peridotite complex, Japan. *Journal of Petrology* 40: 1827–1831.
- 1039
- 1040 Taylor WR (1998) An experimental test of some geothermometer and geobarometer formulations  
1041 for upper mantle peridotites with application to the thermobarometry of fertile lherzolite and garnet  
1042 websterite. *Neues Jahrbuch für Mineralogie, Abhandlungen* 172: 381–408.
- 1043
- 1044 Tommasi A, Vauchez A, Ionov DA (2008) Deformation, static recrystallization, and reactive melt  
1045 transport in shallow subcontinental mantle xenoliths (Tok Cenozoic volcanic field, SE Siberia).  
1046 *Earth and Planetary Science Letters* 272: 65–77, doi: 10.1016/j.epsl.2008.04.020.
- 1047
- 1048 Tommasi A, Ishikawa A (2014) Microstructures, composition, and seismic properties of the Ontong  
1049 Java Plateau mantle root. *Geochemistry, Geophysics, Geosystems*, doi: 10.1002/2014GC005452.
- 1050
- 1051 Van Acken D, Becker H, Walker RJ, McDonough WF, Wombacher F, Ash RD, Piccoli PM (2010)  
1052 Formation of pyroxenite layers in the Totalp ultramafic massif (Swiss Alps)—Insights from highly  
1053 siderophile elements and Os isotopes. *Geochimica et Cosmochimica Acta* 74: 661–683.
- 1054
- 1055 Vannucci R, Shimizu N, Piccardo GB, Ottolini L, Bottazzi P (1993) Distribution of trace-elements  
1056 during breakdown of mantle garnet: an example from Zabargad. *Contributions to Mineralogy and*  
1057 *Petrology* 113: 437–449.
- 1058
- 1059 Villiger S, Ulmer P, Müntener O, Thompson B (2004) The liquid line of descent of anhydrous,  
1060 mantle-derived, tholeiitic liquids by fractional and equilibrium crystallization can experimental  
1061 study at 1.0 GPa. *Journal of Petrology* 45: 2369-2388.

1063 Villiger S, Müntener O, Ulmer P (2007) Crystallization pressures of mid-ocean ridge basalts  
1064 derived from major element variations of glasses from equilibrium and fractional crystallization  
1065 experiments. *Journal of Geophysical Research* 112, doi:10.1029/2006JB004342.  
1066  
1067 Warren JM, Shimizu N, Sakaguchi C, Dick, HJB & Nakamura, E (2009) An assessment of upper  
1068 mantle heterogeneity based on abyssal peridotite isotopic compositions. *Journal of Geophysical*  
1069 *Research* 114: B12203.  
1070  
1071 Warren JM, Shimizu N (2010) Cryptic variations in abyssal peridotite compositions: evidence for  
1072 shallow-level melt infiltration in the oceanic lithosphere. *Journal of Petrology* 51: 395-423, doi:  
1073 10.1093/petrology/egp096.  
1074  
1075 Warren JM (2016) Global variations in abyssal peridotite compositions. *Lithos* 248-251: 193–219,  
1076 doi: 10.1016/j.lithos.2015.12.023.  
1077  
1078 Workman RK, Hart SR (2005) Major and trace element composition of the depleted MORB mantle  
1079 (DMM). *Earth and Planetary Science Letters* 231: 53–72, doi: 10.1016/j.epsl.2004.12.005.  
1080  
1081 Yu S, Xu Y, Ma J, Zheng Y, Kuang Y, Hong L, Ge W, Tong L (2010) Remnants of oceanic lower  
1082 crust in the subcontinental lithospheric mantle: trace element and Sr–Nd–O isotope evidence from  
1083 aluminous garnet pyroxenite xenoliths from Jiaohe, Northeast China. *Earth and Planetary Science*  
1084 *Letters* 297: 413–422.

1085  
1086 **Figure captions**

1087  
1088 **Figure 1:** Representative field occurrences of pyroxenite layers within the Mt. Maggiore peridotitic  
1089 body. A: Partially dissolved pyroxenite layers within country spinel lherzolite; B: Partially  
1090 dissolved spinel pyroxenite; C: Close-up of a partially dissolved spinel websterite. Cpx:  
1091 clinopyroxene, Opx: orthopyroxene; D: Plagioclase pyroxenite within country impregnated  
1092 peridotite; E: Close-up of a plagioclase pyroxenite, showing interstitial plagioclase and  
1093 orthopyroxene enrichments.

1094  
1095 **Figure 2:** Representative microstructures of the spinel and plagioclase pyroxenites. A: Spinel  
1096 pyroxenite. Interstitial olivine develops embayments on porphyroclastic clinopyroxene; B: Spinel

1097 pyroxenite. Interstitial olivine develops embayments on porphyroclastic orthopyroxene; C:  
1098 Plagioclase pyroxenite. Interstitial plagioclase + orthopyroxene intergrowths develops embayments  
1099 on interstitial olivine and porphyroclastic clinopyroxene; D: Plagioclase pyroxenite. Interstitial  
1100 plagioclase and orthopyroxene develop embayments on interstitial olivine and exsolved  
1101 porphyroclastic clinopyroxene; E: Plagioclase pyroxenite. Extensive orthopyroxene exsolution  
1102 development in porphyroclastic clinopyroxene; F: Plagioclase pyroxenite. Interstitial orthopyroxene  
1103 and plagioclase intergrowth at the expense of a porphyroclastic clinopyroxene showing extensive  
1104 [orthopyroxene + plagioclase] exsolutions.

1105  
1106 **Figure 3:** Olivine Crystallographic Preferred Orientation of plagioclase pyroxenites from the Mt.  
1107 Maggiore peridotitic body. One point-per-grain equal-area, lower hemisphere stereographic  
1108 projections. The colour bar is scaled to the maximum concentration of the three crystallographic  
1109 axes. BA refers to the calculated BA-index ([Mainprice et al. 2014](#)).

1110  
1111 **Figure 4:** Major element concentrations of clinopyroxene (A-B) and orthopyroxene (C-D) in spinel  
1112 pyroxenites and plagioclase pyroxenites. A: Mg# (mol%) vs Al<sub>2</sub>O<sub>3</sub> (wt%); B: Na<sub>2</sub>O vs Al<sub>2</sub>O<sub>3</sub>  
1113 (wt%); C: Mg# (mol%) vs Al<sub>2</sub>O<sub>3</sub> (wt%); D: Cr<sub>2</sub>O<sub>3</sub> vs Al<sub>2</sub>O<sub>3</sub> (wt%). Compositional fields of Mt.  
1114 Maggiore spinel and plagioclase peridotites after [Basch et al. \(2018\)](#), and single analyses of spinel  
1115 websterites from South-West Indian Ridge ([Dantas et al. 2007](#)) and plagioclase websterites from  
1116 Lena Trough ([Laukert et al. 2014](#)).

1117  
1118 **Figure 5:** C1-normalized REE composition of rock-forming minerals in the impregnated  
1119 pyroxenites. A: Porphyroclastic clinopyroxene core; B: Porphyroclastic and interstitial  
1120 orthopyroxene core; C: Interstitial plagioclase core. C1-chondrite normalization values after [Sun  
1121 and McDonough \(1989\)](#). Internal Ligurian websterite after [Sanfilippo and Tribuzio \(2011\)](#),  
1122 compositional field for Mt. Maggiore plagioclase peridotites after [Basch et al. \(2018\)](#), plagioclase  
1123 websterite from Lena Trough after [Laukert et al. \(2014\)](#), and spinel websterite 1 and 2 from 9-16°  
1124 South-West Indian Ridge after [Warren et al. \(2009\)](#) and [Dantas et al. \(2007\)](#), respectively.

1125  
1126 **Figure 6:** Total melt fraction (g) vs composition of the single melt increments and aggregated melts  
1127 formed during the pMELTS modeling of DMM mantle ([Workman and Hart 2005](#)) adiabatic  
1128 decompression. A: Mg# (mol%); B: Ca# (mol%); C: Al<sub>2</sub>O<sub>3</sub> (wt%); D: SiO<sub>2</sub> (wt%); E: Na<sub>2</sub>O (wt%);  
1129 F: CaO (wt%). Considered thermal gradient of 0.8°C/km.

1130  
1131  
1132  
1133  
1134  
1135

1131 **Figure 7:** Temperature (°C) vs cumulated modal composition of the assimilated and fractionated  
1132 phases during the pMELTS model of reactive fractional crystallization from 10 kbar, 1360°C to 9  
1133 kbar, 1310°C. Initial melt composition is the single melt increment formed after 6% fractional  
1134 melting of DMM mantle (Table S6). A: Mass (g) of the assimilated and fractionated phases, on the  
1135 basis of 100 grams of melt; B: Modal proportion (vol%) of the assimilated and fractionated phases.

1136  
1137 **Figure 8:** Mg# (mol%) vs Major element concentrations of clinopyroxenes (A-D) and  
1138 orthopyroxenes (E-H) analyzed in Mt. Maggiore pyroxenites and modeled by the pMELTS reactive  
1139 fractional crystallization process. A,E: Al<sub>2</sub>O<sub>3</sub> (wt%); B,F: Na<sub>2</sub>O (wt%); C,G: MgO (wt%); D,H:  
1140 FeO (wt%). Numbers associated to the crystallization trends correspond to crystallization  
1141 temperatures.

1142  
1143 **Figure 9:** Temperature (°C) vs cumulated modal composition of the assimilated and fractionated  
1144 phases during the pMELTS model of reactive porous flow from 8 kbar, 1320°C to 7 kbar, 1290°C.  
1145 Initial melt composition used is the 1335°C melt output from the previous model of reactive  
1146 fractional crystallization (Table S6). A: Mass (g) of the assimilated and fractionated phases, on the  
1147 basis of 100 grams of melt; B: Modal proportion (vol%) of the assimilated and fractionated phases.

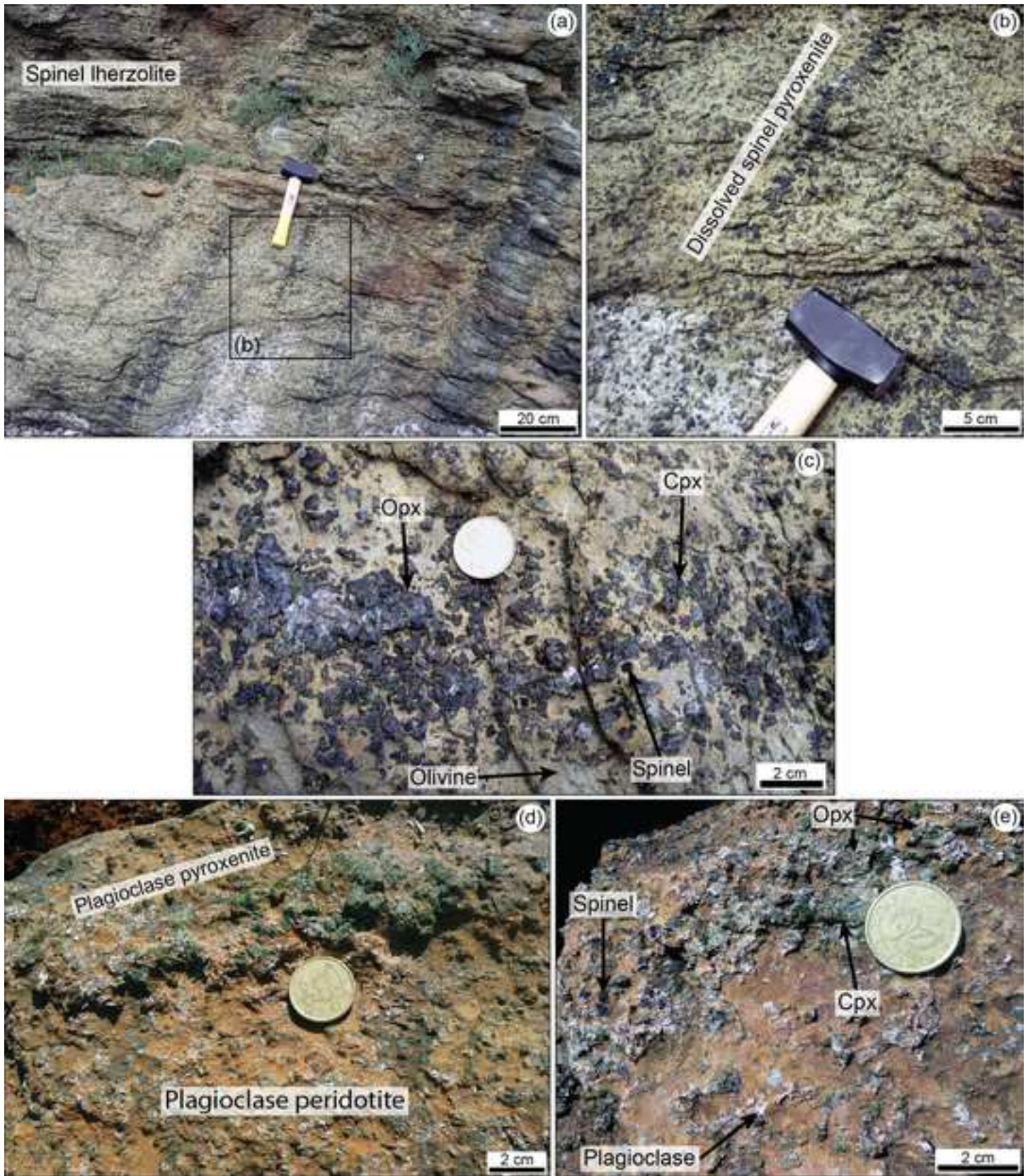
1148  
1149 **Figure 10:** Temperature (°C) vs cumulated modal composition of the assimilated and fractionated  
1150 phases during the pMELTS model of melt impregnation from 7 kbar, 1280°C to 6 kbar, 1200°C.  
1151 Initial melt composition used is the 1290°C melt output from the previous model of reactive porous  
1152 flow (Table S6). A: Mass (g) of the assimilated and fractionated phases, on the basis of 100 grams  
1153 of melt; B: Modal proportion (vol%) of the assimilated and fractionated phases.

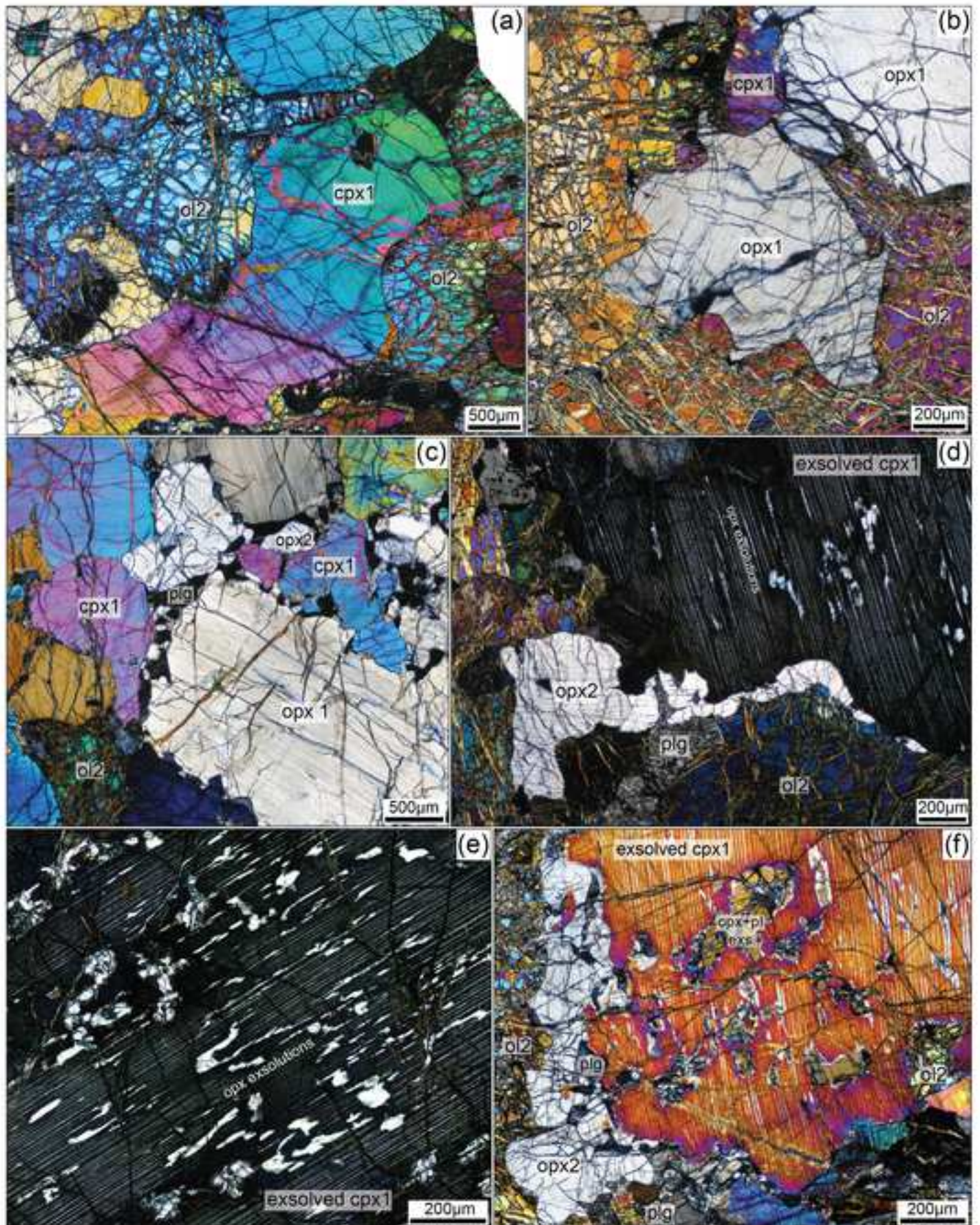
1154  
1155 **Figure 11:** Major element concentrations of orthopyroxenes (Mg# vs A-D) and plagioclase (SiO<sub>2</sub>  
1156 vs E-H) analyzed in Mt. Maggiore pyroxenites and modeled by the pMELTS melt impregnation  
1157 process. A: Al<sub>2</sub>O<sub>3</sub> (wt%); B: Na<sub>2</sub>O (wt%); C: MgO (wt%); D: FeO (wt%); E: An (mol%); F: Na<sub>2</sub>O  
1158 (wt%); G: Al<sub>2</sub>O<sub>3</sub> (wt%); CaO (wt%). Numbers associated to the crystallization trends correspond to  
1159 crystallization temperatures.

1160  
1161 **Figure 12:** Interpretative sketches of the geological context of the Mt. Maggiore peridotitic body.  
1162 A: Context of formation of the pyroxenite layers and melt percolation through a thick lithosphere in  
1163 the Jurassic Ligurian Tethys basin; B: Mantle column representing the different modeled stages

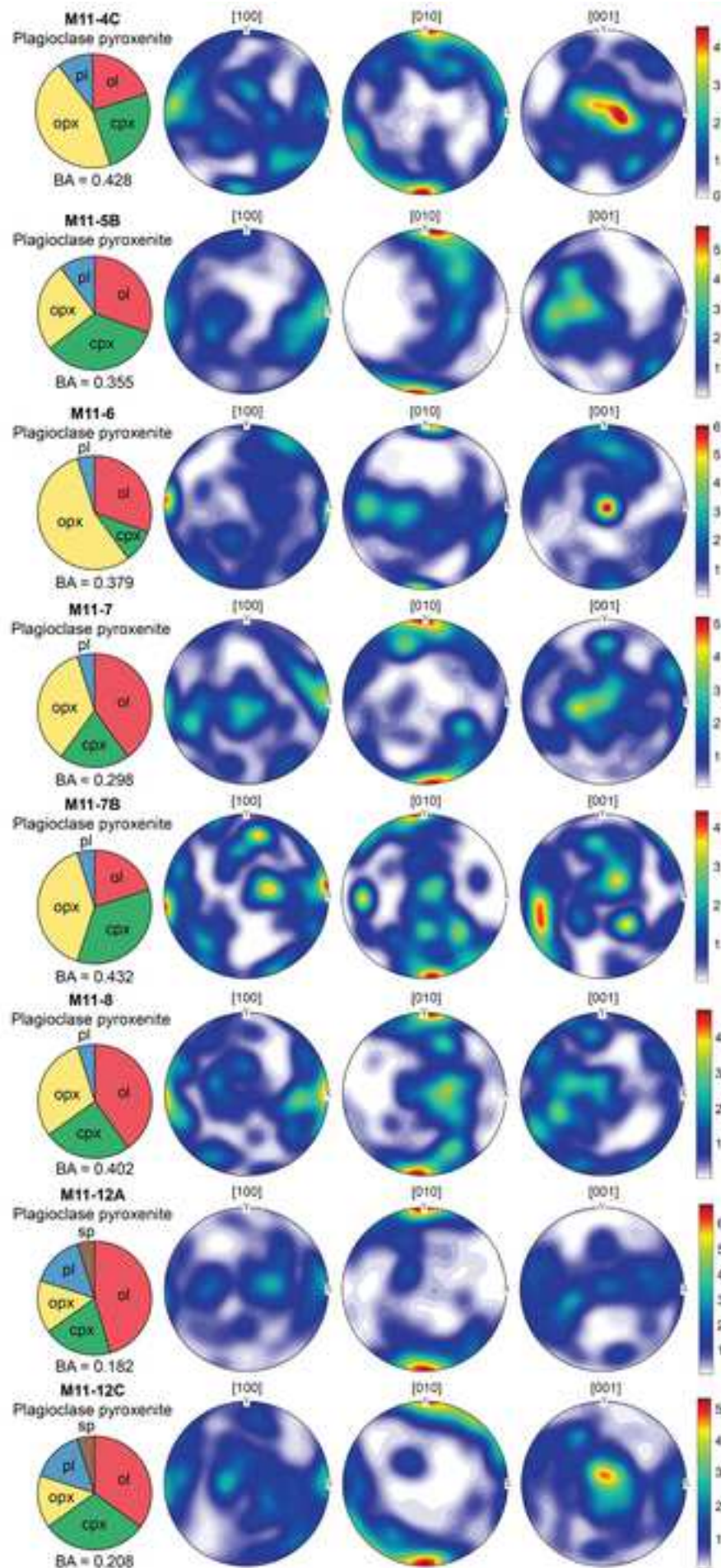
1164 (from mantle melting to spinel-facies reactive percolation to plagioclase-facies melt impregnation;  
1165 see detail in the text).

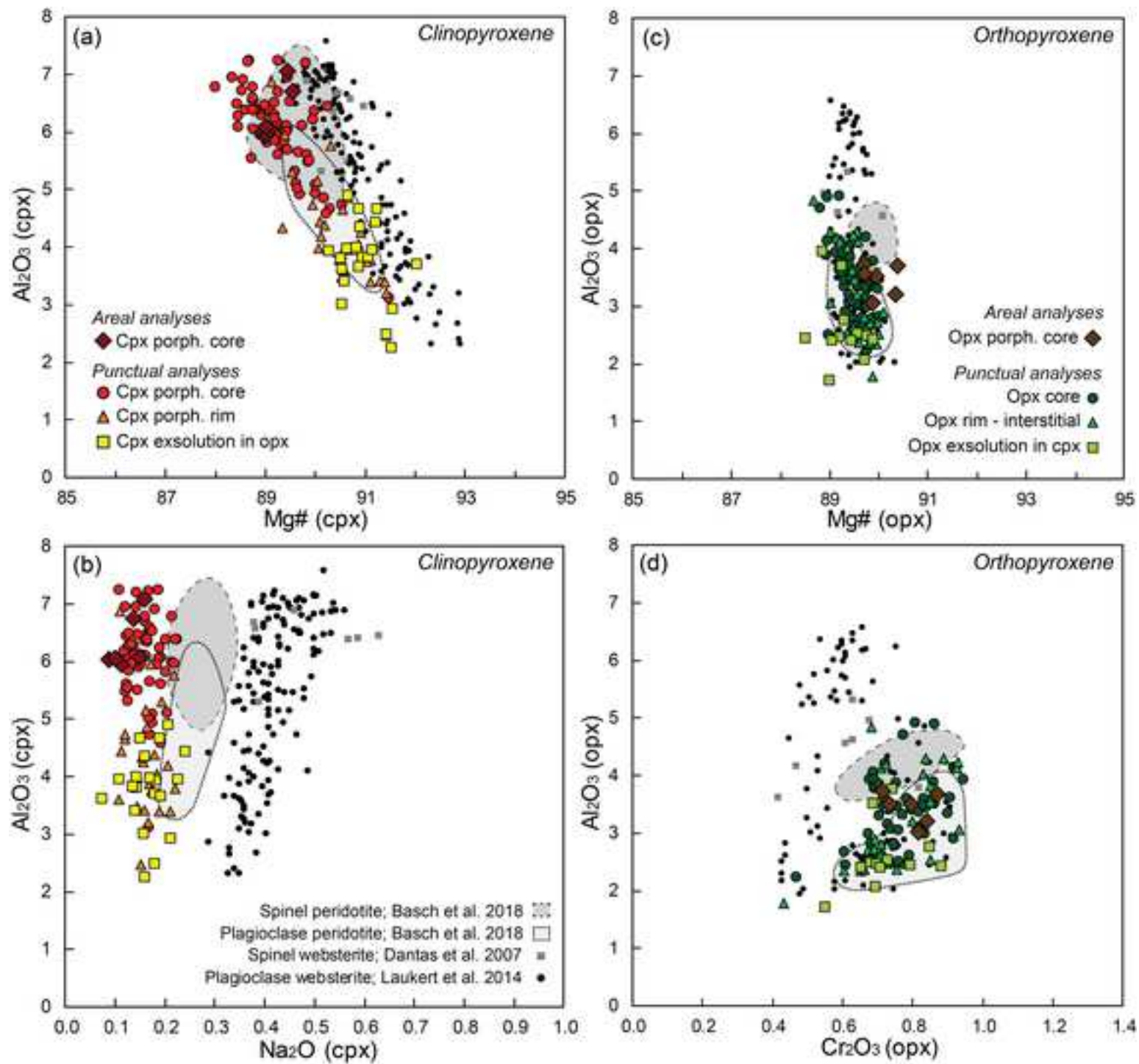
1  
2  
3  
4  
5  
6  
7  
8  
9  
10  
11  
12  
13  
14  
15  
16  
17  
18  
19  
20  
21  
22  
23  
24  
25  
26  
27  
28  
29  
30  
31  
32  
33  
34  
35  
36  
37  
38  
39  
40  
41  
42  
43  
44  
45  
46  
47  
48  
49  
50  
51  
52  
53  
54  
55  
56  
57  
58  
59  
60  
61  
62  
63  
64  
65

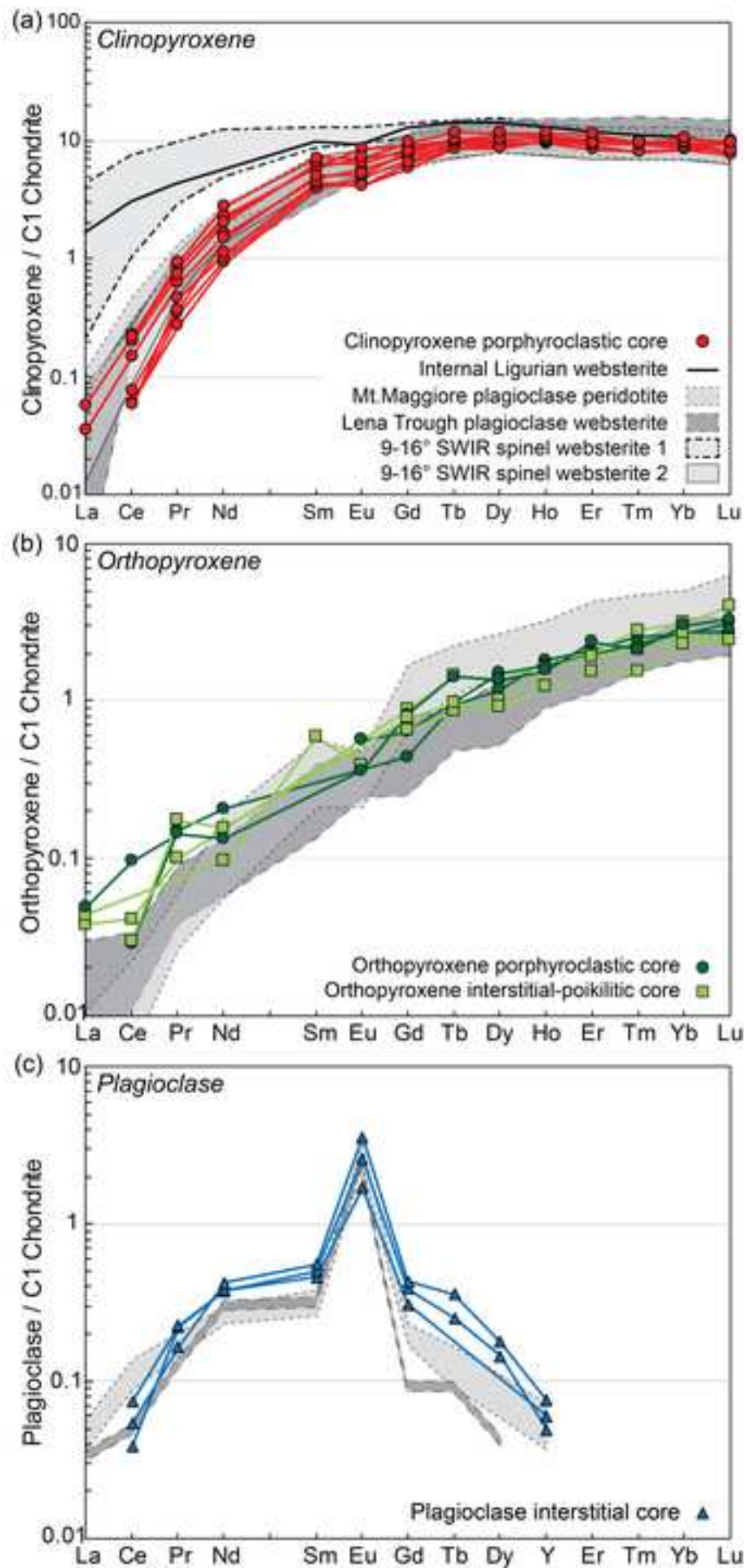


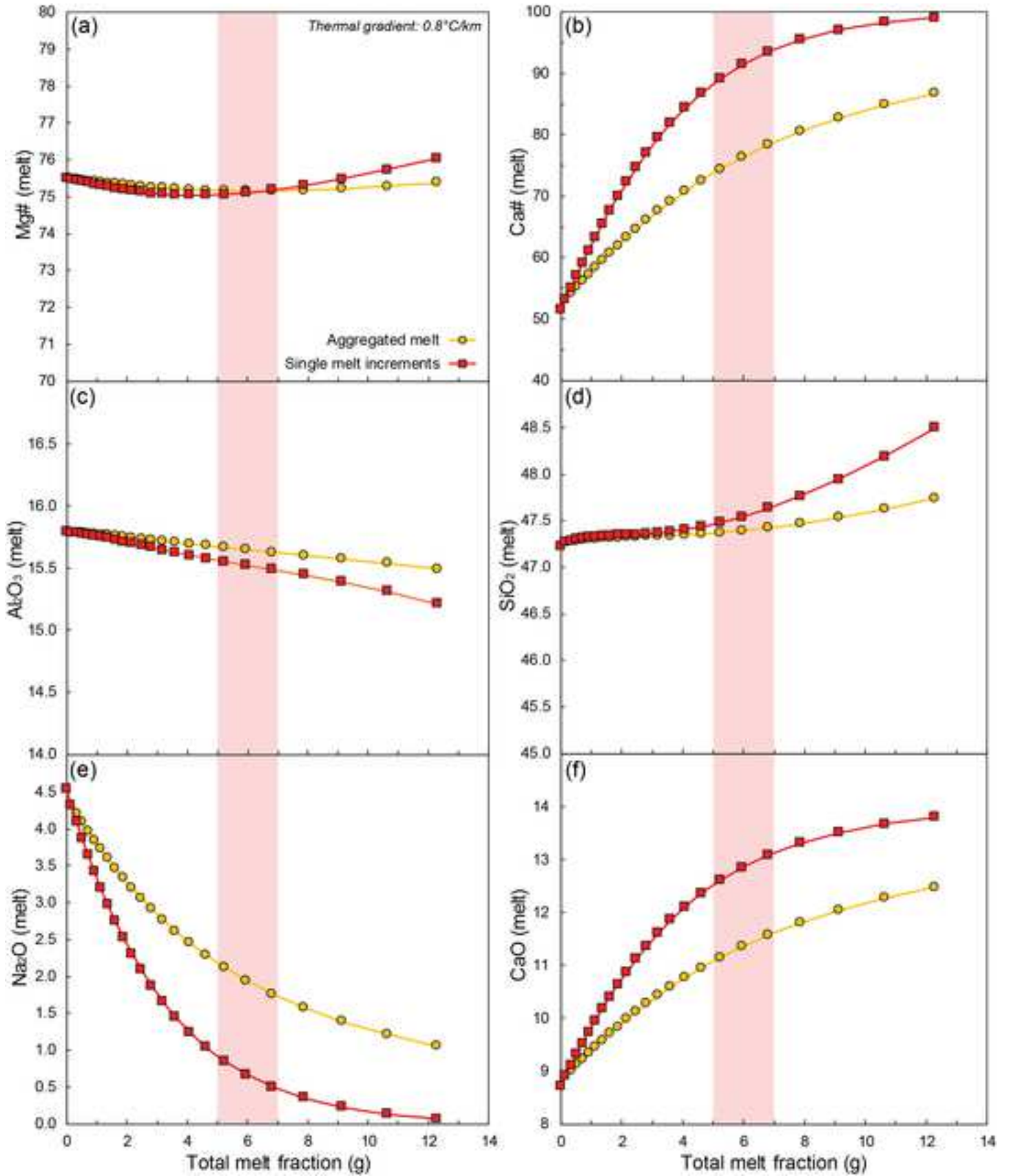


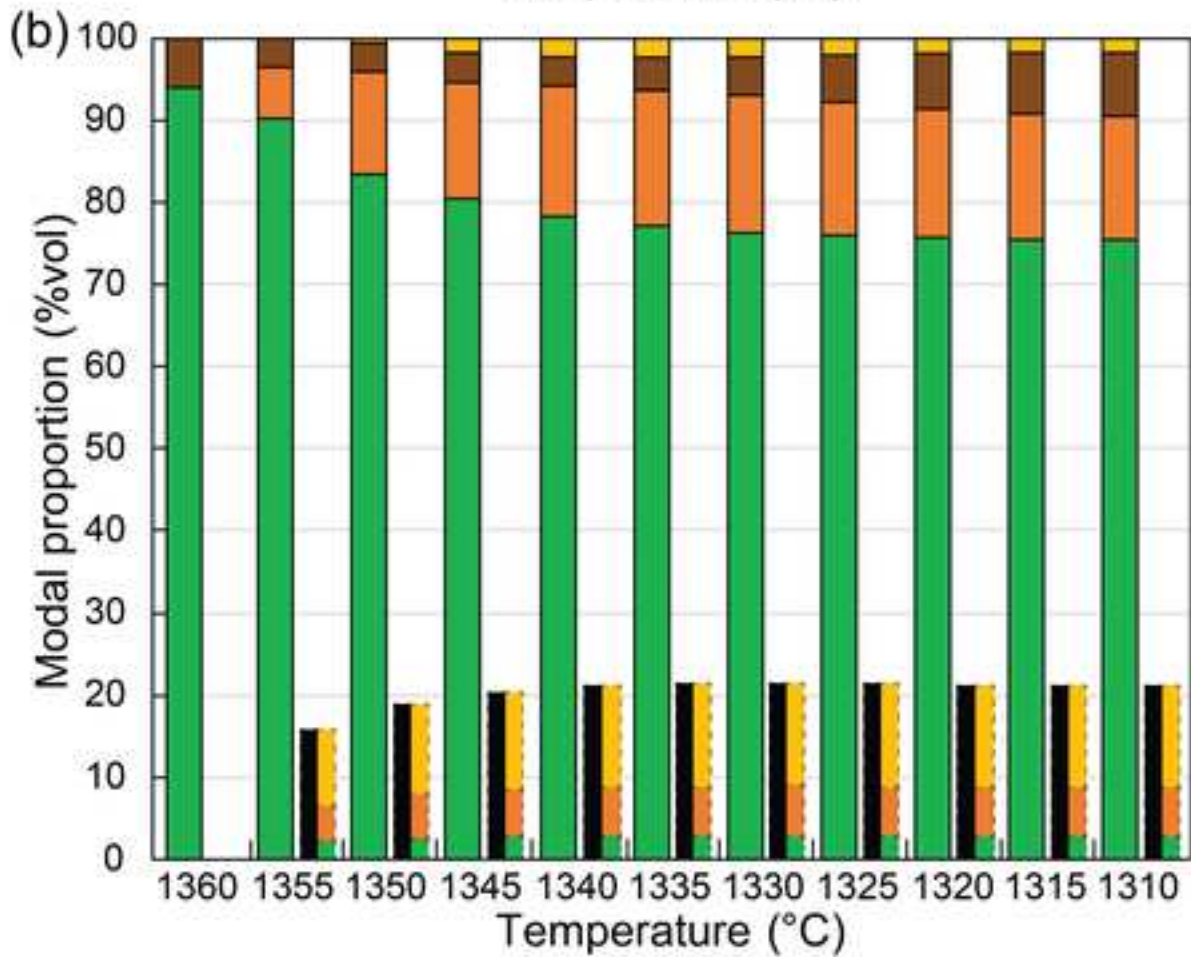
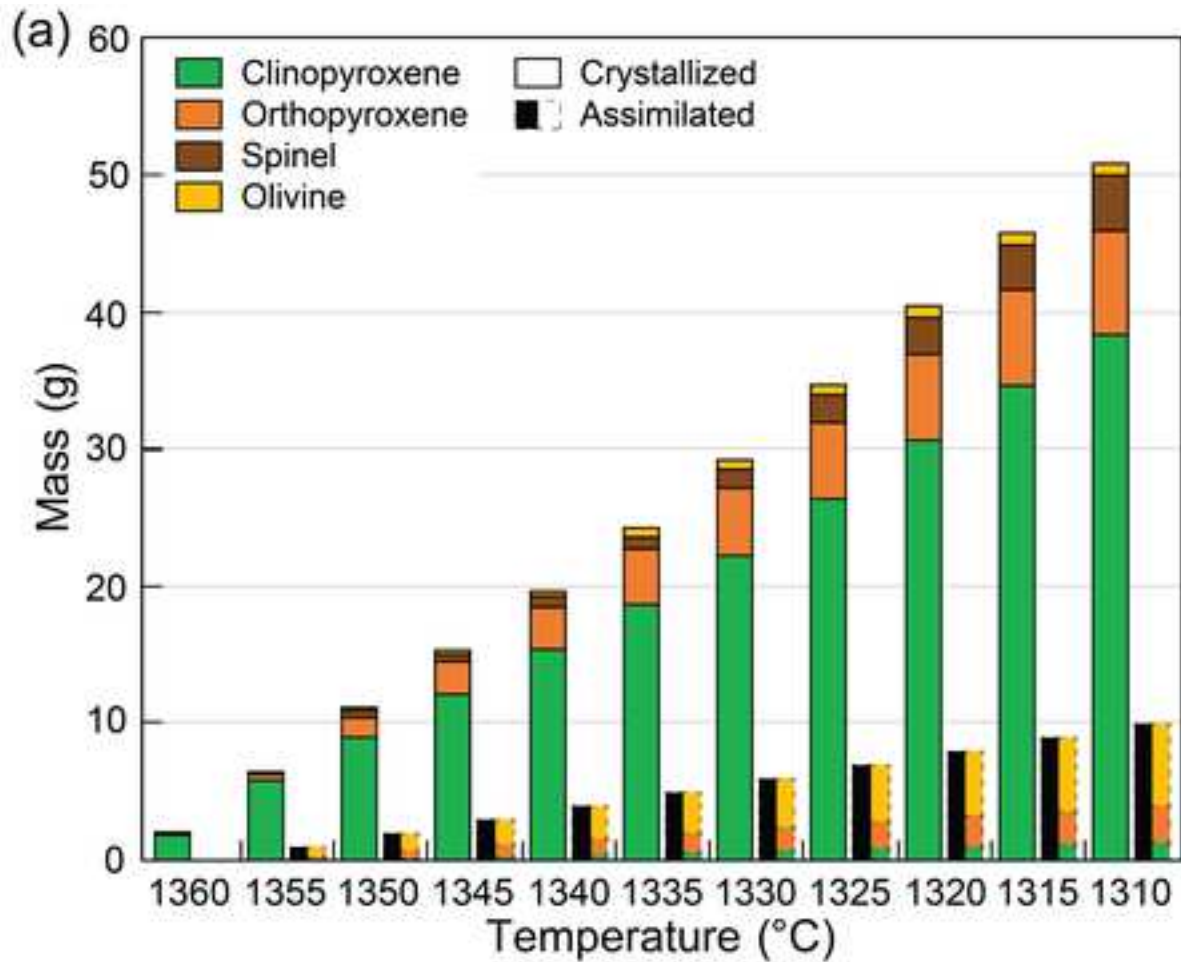


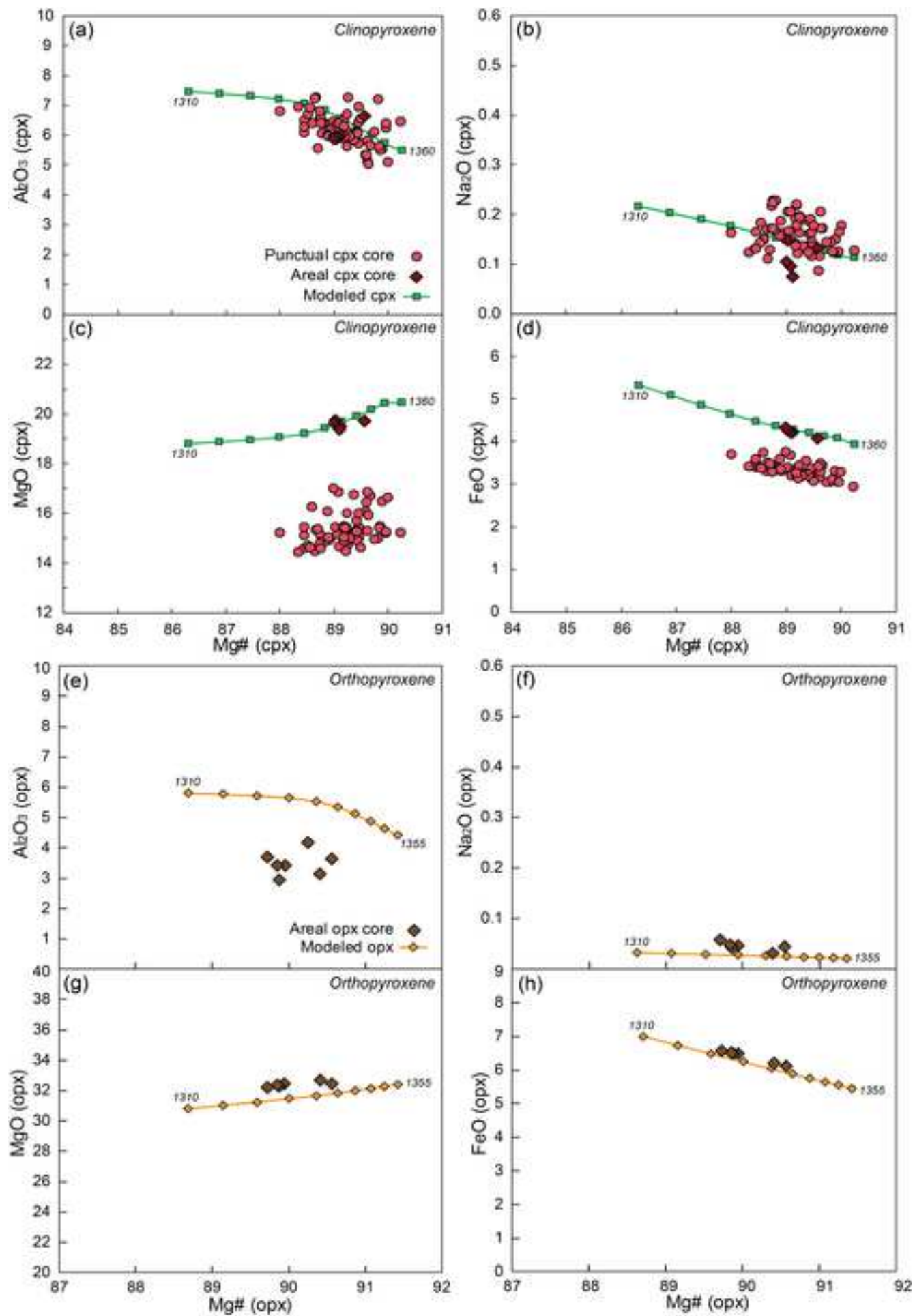


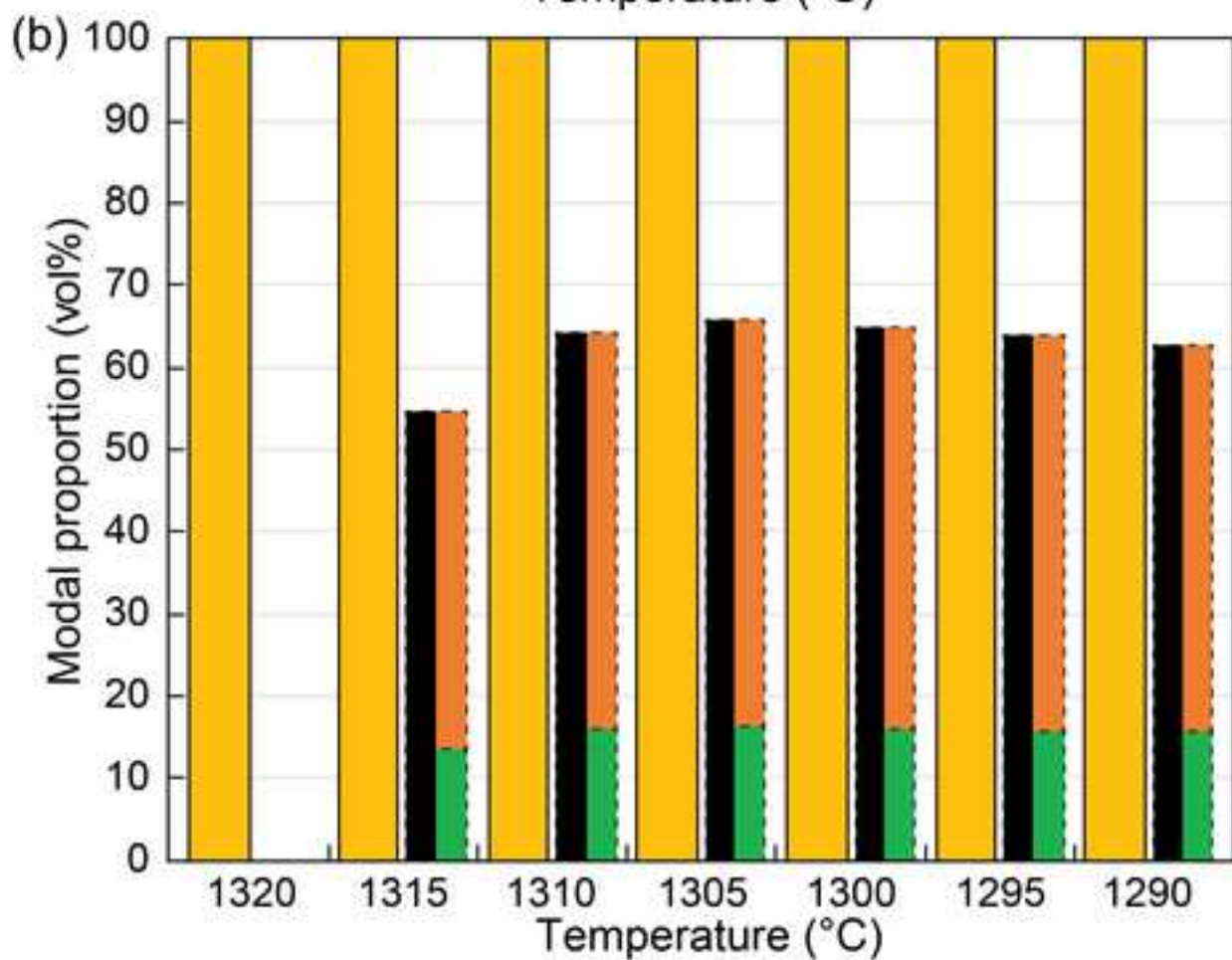
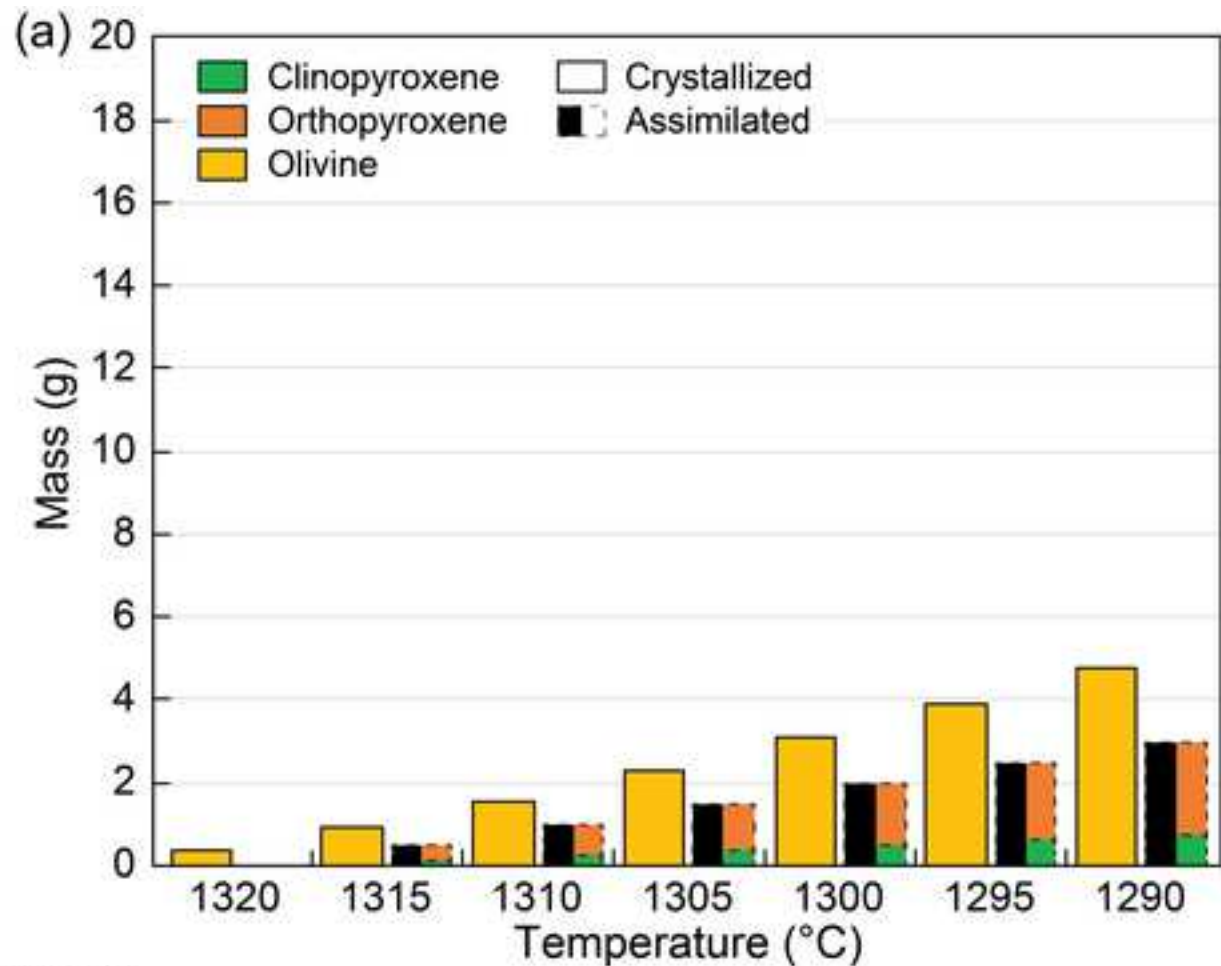


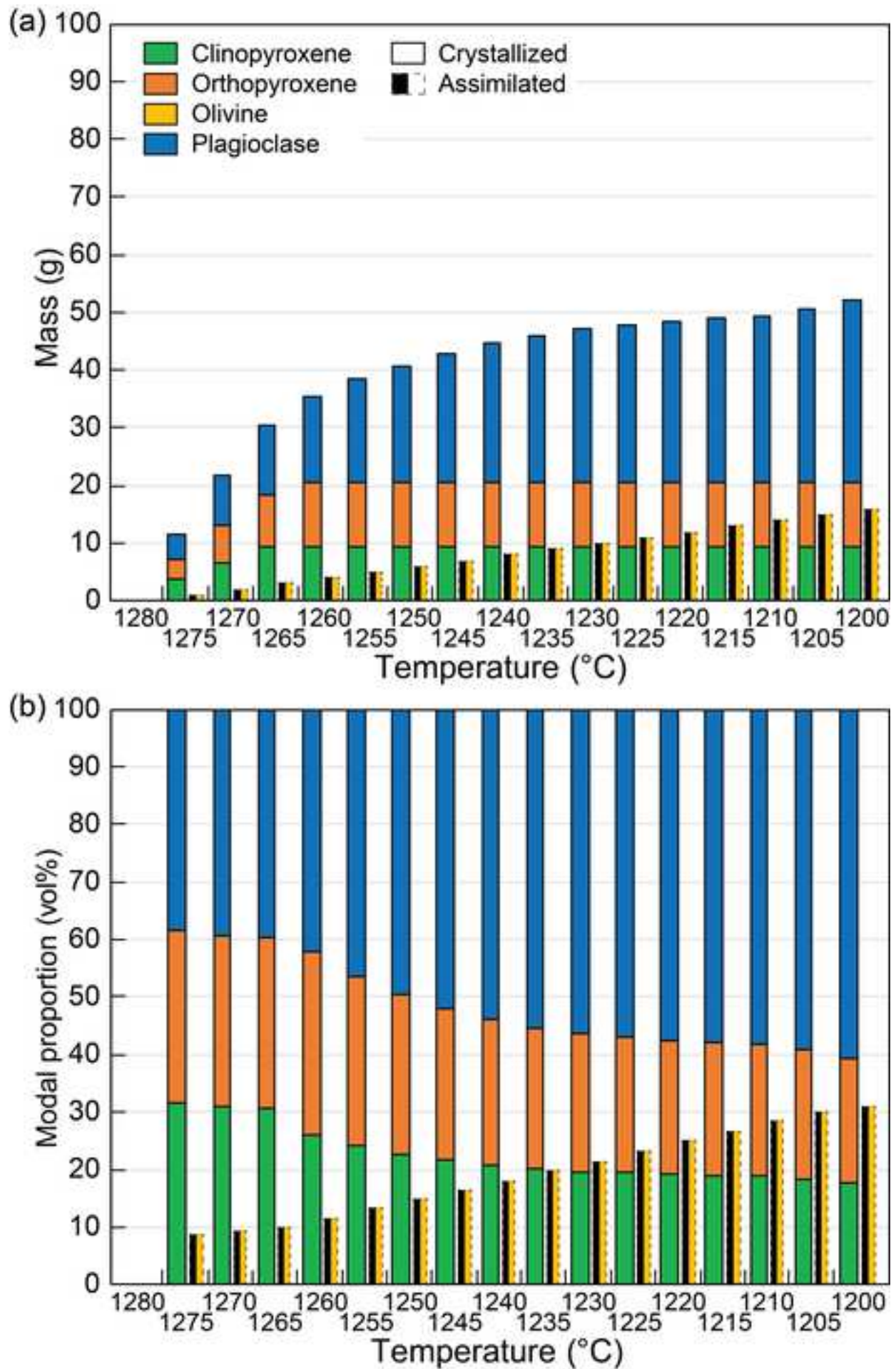




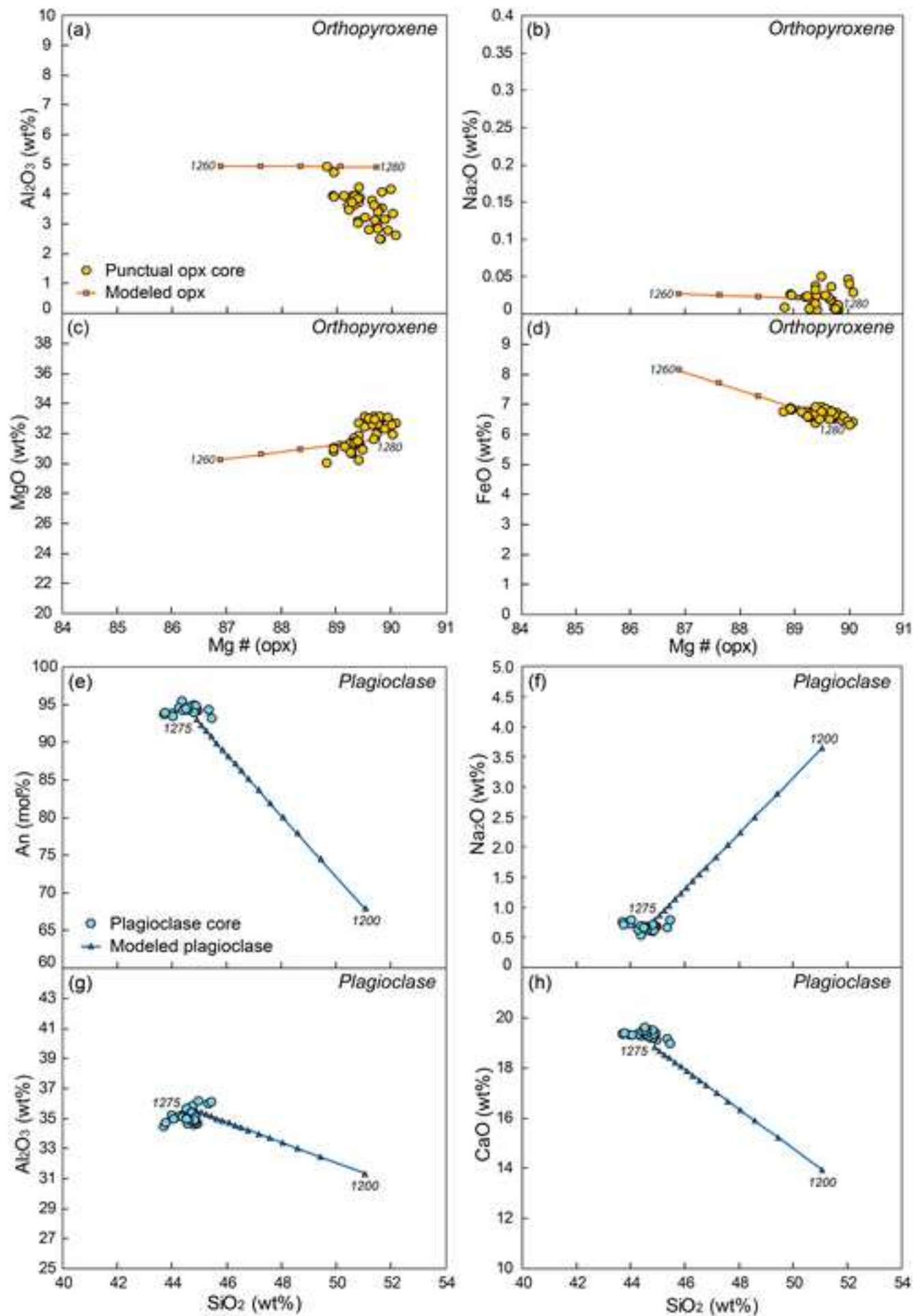












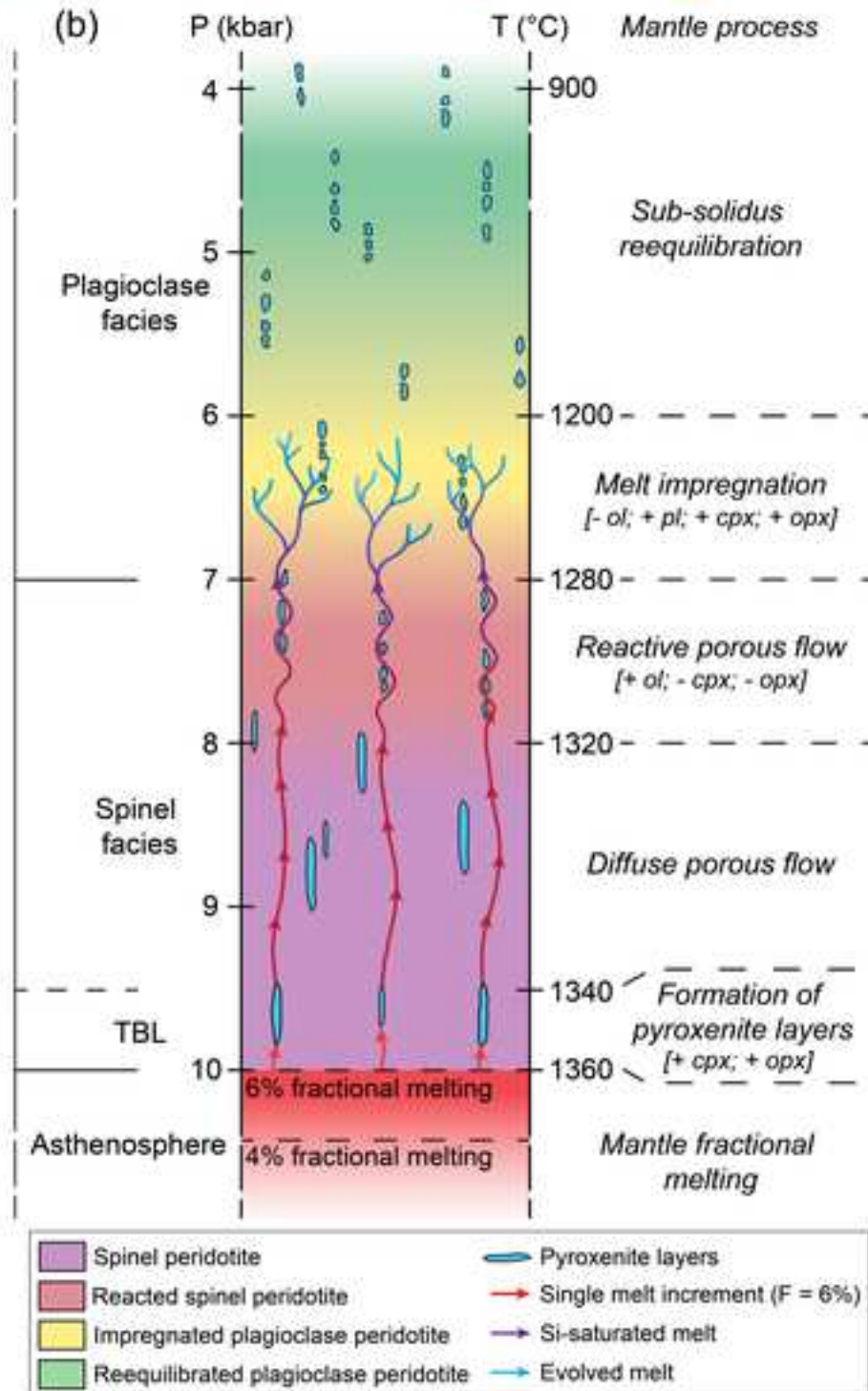
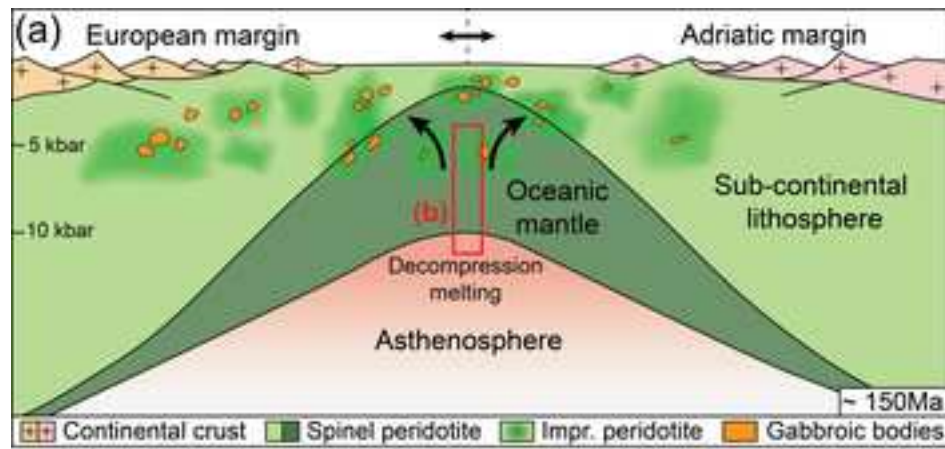


**Table 1:** Studied samples, lithotype, modal composition, BA-index, and PfJ olivine

Sample	Lithotype	Modal compositions (vol%)					EBSD data			
		Ol	Cpx	Opx	Plagio	Sp	BA-index	PfJ [100]	PfJ [010]	PfJ [001]
M11-7B	Spinel pyroxenite	20	35	40	5	0	0.432	2.03	2.25	2.10
M11-4C	Plagioclase pyroxenite	20	25	45	10	0	0.428	1.43	1.81	1.72
M11-5B	Plagioclase pyroxenite	30	35	25	10	0	0.355	2.37	3.87	2.73
M11-6	Spinel pyroxenite	30	10	55	5	0	0.379	1.71	1.96	1.74
M11-8	Spinel pyroxenite	40	25	30	5	0	0.402	2.2	2.27	2.00
M11-12C	Plagioclase pyroxenite	35	30	15	15	5	0.208	1.68	2.55	1.81
M11-7	Spinel pyroxenite	40	20	35	5	0	0.298	1.72	2.35	1.65
M11-12A	Plagioclase pyroxenite	45	20	15	15	5	0.182	1.56	2.74	1.85

Ol: Olivine; Cpx: Clinopyroxene; Opx: Orthopyroxene; Plagio: Plagioclase; Sp: Spinel;  
 PfJ: Fabric strength of single crystallographic pole.

**Table 2:** Geothermobarometric estimates of different processes recorded in the pyroxenite layers. See the text for more detail.

	Temperature (°C)		Pressure (kbar)
	opx-cpx <sup>1</sup>	opx <sup>2</sup>	cpx-opx-pl-ol <sup>3</sup>
Formation of pyroxenites	1210-1240	1260-1300	-
Melt impregnation	-	1080-1290	6.4-6.6
Sub-solidus reequilibration	880-1050	900-1080	4.2-4.6
Extensive sub-solidus reequ.	780-900	900-980	2.9-3.1

<sup>1</sup>after [Brey and Kohler \(1990\)](#) and [Taylor \(1998\)](#);

<sup>2</sup>after [Taylor \(1998\)](#);

<sup>3</sup>after [Fumagalli et al. \(2017\)](#).

**Table 3:** Initial melt compositions used in the pMELTS thermodynamic models of reactive percolation.

Melt composition	T (°C)	P (kbar)	SiO <sub>2</sub>	TiO <sub>2</sub>	Al <sub>2</sub> O <sub>3</sub>	Fe <sub>2</sub> O <sub>3</sub>	Cr <sub>2</sub> O <sub>3</sub>	FeO	MnO	MgO	NiO	CaO	Na <sub>2</sub> O	Total	Mg#	Ca#
Pyrox. Formation	1362.5	10	47.54	0.81	15.52	0.84	0.05	8.06	0.01	13.64	0.01	12.86	0.67	100.0	75.10	91.40
Reac. porous flow	1335	9.75	46.73	0.91	17.04	1.33	0.00	8.46	0.02	12.55	0.02	12.14	0.80	100.0	72.57	89.37
Melt impregnation	1290	7.00	47.48	0.92	17.39	1.35	0.00	8.21	0.00	11.38	0.00	12.45	0.81	100.0	71.19	89.51

Mg# = Mg / (Mg+Fe); Ca# = Ca / (Ca+Na).

[Click here to view linked References](#)

UNIVERSITA' DEGLI STUDI DI GENOVA  
DISTAV  
DIPARTIMENTO DI SCIENZE  
DELLA TERRA, DELL'AMBIENTE  
E DELLA VITA  
Corso Europa, 26, 16132 GENOVA

Elisabetta RAMPONE  
[betta@dipteris.unige.it](mailto:betta@dipteris.unige.it)  
+39 335 224 890

Genova, July 8<sup>th</sup>, 2019

Dear Prof. Müntener,

Please find enclosed the manuscript "**Origin of pyroxenites in the oceanic mantle and their implications on the reactive percolation of depleted melts**", by

**Basch Valentin<sup>1</sup>; Rampone Elisabetta<sup>1</sup>; Borghini Giulio<sup>2</sup>; Ferrando Carlotta<sup>3</sup>; Zanetti Alberto<sup>4</sup>**

<sup>1</sup>Dipartimento di Scienze della Terra, dell'Ambiente e della Vita, University of Genova, Italy;

<sup>2</sup>Dipartimento di Scienze della Terra "Ardito Desio", University of Milano, Italy;

<sup>3</sup>CRPG, University of Lorraine, Nancy, France;

<sup>4</sup>CNR-IGG, Sezione di Pavia, Italy.

that we wish to submit for publication on **Contributions to Mineralogy and Petrology**.

The manuscript reports a combined field, microstructural and geochemical investigation of pyroxenites layers associated to residual oceanic mantle. These pyroxenites formed by high-pressure fractionation of unaggregated depleted melt increments, prior to a melt-rock interaction history related to the reactive percolation of the depleted melts in a thick lithosphere. In this contribution, we model the major element composition of the melt and fractionated phases during formation of depleted melts by mantle melting, high-pressure fractionation of pyroxenites, reactive porous flow and melt impregnation, using pMELTS thermodynamic program.

Major outcomes of this study are: 1) the formation of the pyroxenites as early segregates from unaggregated depleted melts; 2) the necessity of pyroxene fractionation prior to the documented melt-rock interaction history, thus accounting for the "pyroxene paradox"; 3) the demonstration of the continuous evolution of reactive processes and chemical composition of depleted melts during upward migration in a thick Thermal Boundary Layer.

We hope you will consider the subject of interest for publication on **Contributions to Mineralogy and Petrology** and look forward hearing from you. In the following is a list of suggested reviewers:

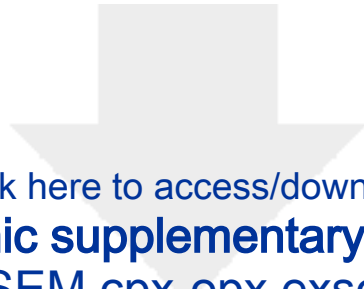
**Sébastien Pilet** (sebastien.pilet@unil.ch)

**Georges Ceuleneer** (georges.ceuleneer@get.omp.eu)

**Claudio Marchesi** (claudio@iact.ugr-csic.es)

Best regards

Elisabetta Rampone



[Click here to access/download](#)

**Electronic supplementary material**

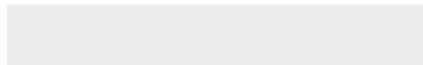
Figure S1 SEM cpx-opx exsolutions.png



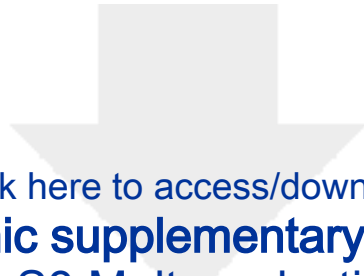


[Click here to access/download](#)

**Electronic supplementary material**  
Figure S2 REE modeling fusion.png







Click here to access/download  
**Electronic supplementary material**  
Figure S3 Melt production.png

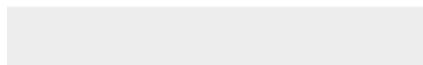




[Click here to access/download](#)

**Electronic supplementary material**

Figure S4 Modal compositions without pyroxenite.png





[Click here to access/download](#)

**Electronic supplementary material**  
Figure S5 AFC pyroxenites REE.png

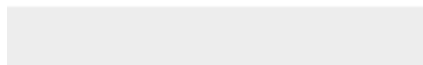


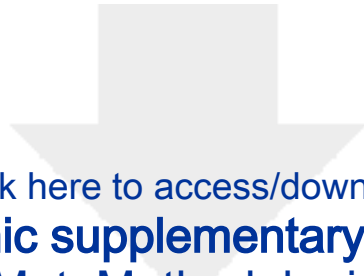


[Click here to access/download](#)

**Electronic supplementary material**

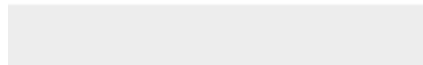
Figure S6 P-T evolution Mt.Maggiore.png





Click here to access/download

**Electronic supplementary material**  
Suppl.Mat. Methodologies.docx



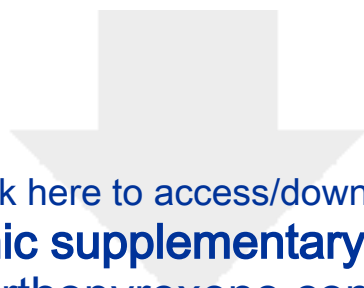


[Click here to access/download](#)

**Electronic supplementary material**

Table S1 - Clinopyroxene composition.xlsx



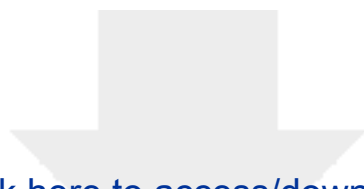


[Click here to access/download](#)

**Electronic supplementary material**

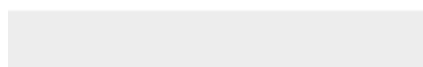
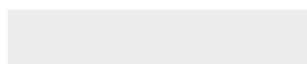
Table S2 - Orthopyroxene composition.xlsx





Click here to access/download

**Electronic supplementary material**  
Table S3 - Plagioclase composition.xlsx



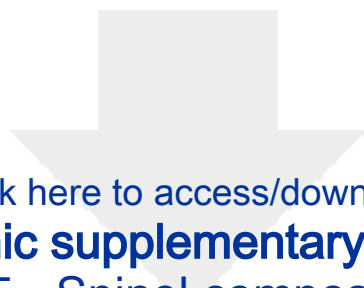




[Click here to access/download](#)

**Electronic supplementary material**  
**Table S4 - Olivine composition.xlsx**

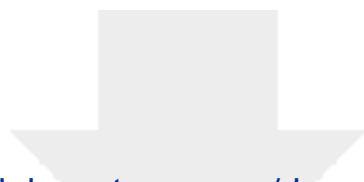




[Click here to access/download](#)

**Electronic supplementary material**  
**Table S5 - Spinel composition.xlsx**





[Click here to access/download](#)

**Electronic supplementary material**  
Table S6 - Detail pMELTS models.xlsx

